Nonlinear transport phenomena and current-induced hydrodynamics in ultrahigh mobility two-dimensional electron gas

Z. T. Wang,[1] M. Hilke [1,*] N. Fong [2] D. G. Austing,[1,2,†] S. A. Studenikin [2] K. W. West,[3] and L. N. Pfeiffer[3]

[1]*Department of Physics, McGill University, Montréal, Quebec H3A 2T8, Canada*
[2]*Emerging Technology Division, National Research Council of Canada, Ottawa, Ontario K1A 0R6, Canada*
[3]*Department of Electrical Engineering, Princeton University, Princeton, New Jersey 08544, USA*

We report on nonlinear transport phenomena at high filling factor and DC current-induced electronic hydro-dynamics in an ultrahigh mobility ($\mu = 20 \times 10^6$ cm^2/Vs) two-dimensional electron gas in a narrow ($15 - \mu$m wide) GaAs/AlGaAs Hall bar for DC current densities reaching 0.67 A/m. The various phenomena and the boundaries between the phenomena are captured together in a two-dimensional differential resistivity map as a function of magnetic field (up to 250 mT) and DC current. This map, which resembles a phase diagram, demarcate distinct regions dominated by Shubnikov-de Haas (SdH) oscillations (and phase inversion of these oscillations) around zero DC current; negative magnetoresistance and a double-peak feature (both ballistic in origin) around zero field; and Hall field-induced resistance oscillations (HIROs) radiating out from the origin. From a detailed analysis of the data near zero field, we show that increasing the DC current suppresses the electron-electron scattering length that drives a growing hydrodynamic contribution to both the differential longitudinal and transverse (Hall) resistivities. Our approach to induce hydrodynamics with DC current differs from the more usual approach of changing the temperature. We also find a significant (factor of two to four) difference between the quantum lifetime extracted from SdH oscillations, and the quantum lifetime extracted from HIROs. In addition to observing HIRO peaks up to the seventh order, we observe an unexpected HIRO-like feature close to midway between the first-order and the second-order HIRO maxima at high DC current.

I. INTRODUCTION

High mobility two-dimensional electron gas (2DEG) systems exhibit a remarkable richness of phenomena. In a strong magnetic (B) field there are various topological phases such as integer and fractional quantum Hall phases, which stem from an interplay of disorder, electron correlations, and B field. These phases are distinguished by their Hall quantization [1,2]. On the other hand, nonlinear phenomena, such as Hall field-induced, phonon-induced, and microwave-induced resistance oscillations, in Landau levels (LLs) at high filling factor close to zero B field are examples of phenomena that cannot be characterized by conductance quantization. These nonlinear phenomena have attracted significant interest over the last two decades (see the extensive reviews in Refs. [3,4] and references therein).

Regarding nonlinear DC transport, the principal topic of our paper, the quintessential example of a DC current-induced phenomenon at low B field is Hall field-induced resistance oscillations (HIROs) [5]. In published experimental works on HIROs [5–19], typically data are presented in the form of selected traces of differential resistance versus B field at fixed DC current (or differential resistance versus DC current at fixed B field). Such an approach may not reveal all aspects

of HIROs or HIRO-like phenomena, and their relationship to other distinct linear and nonlinear phenomena at low B field may not be clear. An alternative approach to gain a more complete picture is to map out the resistance as a function of B field and DC current. Such a technique has been applied at high magnetic field in the quantum Hall regime and demon-strated to reveal a wealth of phenomena (see Refs. [20–24]).

Recently viscous transport in two-dimensional (2D) systems has also drawn significant interest. Hydrodynamic phenomena are expected to be most pronounced when the (momentum-conserving) electron-electron scattering length l_{ee} is much less than the device width W, and in turn, W is much less than the classical transport mean free path l_{mfp}, i.e., $l_{ee} \ll W \ll l_{mfp}$, distinct to the condition $W \ll l_{ee}, l_{mfp}$ for which ballistic effects dominate. The subject of hydrodynamic effects in solids at low temperature was pioneered by Gurzhi in the 1960's [25,26], and initially drew theoretical attention, see for example Refs. [27–31]. With the advent of materials in the 1990's for which (momentum-relaxing) scattering with defects and phonons was sufficiently weak, Molenkamp and de Jong investigated experimentally hydrodynamic electron flow in high-mobility GaAs/AlGaAs heterostructure wires, and could distinguish the Knudsen and Poiseuille (Gurzhi) transport regimes in the differential resistance [30–32]. Two decades ago analogies with fluid dynamics were also explored to explain voltage steps in the quantum Hall effect breakdown regime including an eddy viscosity model for the disrup-tion of laminar flow around charged impurities [33–38]. In

*hilke@physics.mcgill.ca
†guy.austing@nrc-cnrc.gc.ca

recent years there has been renewed interest in hydrodynamic electron transport following the development of material systems with ever higher transport mean free path. Experimental works studying hydrodynamic effects in 2D systems feature graphene [39–49], high-mobility semiconductor 2DEGs [50–60], 2D metals [61], semimetals [62], and semimetal microribbons [63]. This effort has inspired numerous theoretical works of which Refs. [58,64–73] are examples of those focusing on semiconductor 2DEGs. Change of temperature to suppress l_{ee} is the most common approach to reach the hydrodynamic regime, although channel thinning in steps to effectively change W can be employed in certain instances as in Ref. [61]. It was also predicted in Ref. [27] that l_{ee} decreases with increasing DC current, which is the basis of current-induced viscous transport as originally investigated by Molenkamp and de Jong [30–32], see also Ref. [74].

Here, we examine in detail the differential resistance of an ultrahigh mobility 2DEG in a narrow Hall bar fabricated from a GaAs/AlGaAs quantum well heterostructure as a function of B field and DC current. This approach allows us to study numerous phenomena in one global 2D diagram as they evolve with increasing DC current up to 10 μA for B fields up to 0.25 T. In the differential longitudinal resistivity, we observe: Shubnikov-de Haas (SdH) oscillations and phase inversion (PhI) of SdH oscillations near zero current, negative magnetoresistance (nMR), and a double-peak feature near zero field, and HIROs up to the seventh order. In addition, we find evidence for DC current-induced electron hydrodynamics effects for B fields less than 10 mT in both the differential longitudinal and transverses resistivities. Since the global 2D diagram (which identifies distinct regions within which different phenomena dominate) resembles a phase diagram in appearance, we will henceforth refer to the diagram as a "phase diagram". There are two main points of our paper. First, the global 2D phase diagram we measure for an ultrahigh mobility 2DEG not only shows the numerous constituent transport regimes *together* in unprecedented detail, but only by considering *all* the transport regimes have we gained detailed information or new insight. For example, the nMR and hydrodynamic regimes cohabit the same region in the phase diagram so the former must be accounted for when examining the latter; the electron temperature extracted from SdH and PhI is relevant to current-induced hydrodynamics; quantities such as the quantum lifetime extracted from different regimes (SdH and HIROs) and usually presumed to be the same are in fact different; and a high-resolution phase diagram can show unexpected features not previously observed (additional HIRO-like features). Second, we demonstrate the hydrodynamic contribution can be increased by applying a DC current rather than by changing the temperature as more generally used. Increasing the DC current reduces the electron-electron scattering length sufficiently that this length becomes comparable to or even smaller than the effective width of the Hall bar.

This paper is organized into five sections. Section II describes the experimental details pertaining to the 2DEG material, the Hall bar device, and the measurement configuration. Section III presents the differential resistivity map, and introduces the different phenomena observed and delineates the boundaries between the phenomena in the phase

TABLE I. Key parameters of the 2DEG material system. The (bulk) parameters given are determined from a large area Van der Pauw device measured in a helium-3 cryostat at base temperature after illumination.

n (cm^{-2})	μ (cm^2/V s)	E_F (meV)	l_{mfp} (μm)
2.0×10^{11}	20×10^6	7.2	145

diagram. Sections IV and V give extensive analysis of the phenomena that are the principal focus of this paper. In more detail, Sec. IV presents analysis, based on current theories for viscous transport, of the observed evolution of both the differential longitudinal and transverse (Hall) resistivities near 0 T with respect to the DC current, which we attribute to hydrodynamic flow. In Sec. V, we compare properties of the HIROs observed in the experiment to those expected from existing theories, and extract various parameters such as the quantum lifetime and the electronic width. We also report an unexpected additional HIRO-like feature in the phase diagram located in between the first-order and the second-order HIROs peak. We end with a conclusion in Sec. VI. The Appendices include supplementary information regarding parameters of interest such as the quantum lifetime extracted from the SdH oscillations; a simulation of the PhI of the SdH oscillations; and evidence that the origin of the nMR and the double-peak feature is purely ballistic in nature.

II. EXPERIMENTAL DETAILS

The Hall bar device is made from a 2DEG confined in a GaAs/AlGaAs quantum well (QW) heterostructure grown by molecular beam epitaxy. The 2DEG is located in a 30-nm-wide GaAs QW at a depth ∼200 nm below the surface. The barriers on either side of the QW are composed of $Al_{0.3}Ga_{0.7}As$ and incorporate QW doping regions. From a large area Van der Pauw device measured in a helium-3 cryostat at base temperature after illumination, the 2DEG sheet density n and (transport) mobility μ respectively for this material are found to be 2.0×10^{11} cm^{-2} and 20×10^6 cm^2/V s. The corresponding Fermi energy E_F and transport mean free path l_{mfp} respectively are determined to be 7.2 meV and 145 μm. These parameters are tabulated in Table I.

The Hall bar device is made by standard fabrication techniques. The nominal (lithographic) width W of the Hall bar is 15 μm. The separation between adjacent voltage probes along each side of the Hall bar is 50 μm. An image of the central region of the device is shown in Fig. 1. For all experiments described, a DC current I_{DC} is combined with an AC excitation current I_{AC} of 20 nA (unless otherwise stated) at 148 Hz, and the net current I_{SD} is driven through the Hall bar from the source contact to the grounded drain contact. ΔV_{xx}, the change in AC voltage along the Hall bar, and ΔV_{xy}, the change in AC voltage across the width of the Hall bar, are measured with a standard lock-in technique and the differential longitudinal and transverse resistances respectively are given by $r_{xx} = \Delta V_{xx}/I_{AC} = dV_{xx}/dI$ and $r_{xy} = \Delta V_{xy}/I_{AC} = dV_{xy}/dI$ (see Refs. [24,76] for further details of the technique).
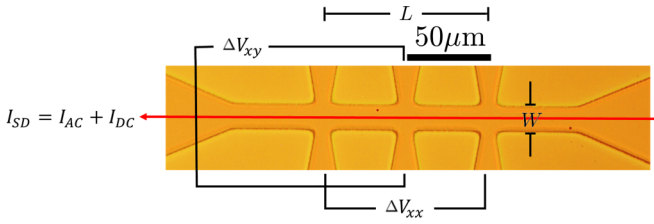
FIG. 1. Image of central region of the Hall bar device showing the measurement configuration. The Ohmic contacts are out of view. The lithographic width of the Hall bar is $W = 15$ μm, and the two voltage probes employed to measure ΔV_{xx} are separated by distance $L = 100$ μm.

Voltages ΔV_{xx} and ΔV_{xy} are measured between the voltage probes indicated in Fig. 1. Note ΔV_{xx} is dropped between voltage probes separated by a distance $L = 100$ μm. Although not measured, a DC voltage drop is also discussed and estimated in Sec. IV. The differential longitudinal and transverse resistivities respectively are $\rho_{xx} = W r_{xx}/L$ and $\rho_{xy} = r_{xy}$. All measurements are performed in the dark in a dilution refrigerator at base temperature where the mixing chamber temperature is ~ 15 mK. The electron temperature T_e is estimated in separate measurements to be ~ 40 mK at zero DC current from the temperature dependence of resistance minima at fractional filling between filling factors one and two. The B field is applied perpendicular to the plane of the 2DEG. Note that a small 6-mT correction has been applied to the data to account for a field offset.

III. PHENOMENA OBSERVED IN THE DIFFERENTIAL RESISTIVITY

We start by looking at the global phase diagram and identify all the different phenomena therein. This is accomplished by measuring ρ_{xx} on sweeping the DC current and stepping the B field. The resulting map is presented in Fig. 2(a). In our Hall bar device, we can identify several phenomena of interest: SdH oscillations, phase inverted SdH oscillations, nMR, a double peak-feature on top of the nMR, DC current-induced hydrodynamic effects, HIROs, and a HIRO-like feature. In the rest of this section we provide a general introduction to these phenomena before going into detail. To aid this introduction, Fig. 2(f) provides a simple schematic showing the regions, in one quadrant of the phase diagram, where the phenomena are observed, the boundaries between the phenomena, and characteristic B fields and DC currents.

SdH oscillations at zero DC current are observed above 21 mT and their amplitude in differential resistivity is found to decay with increasing I_{DC} (see additionally both Figs. 9 and 10 in Appendix A). In general, SdH oscillations are absent when $\omega_c \tau_q \ll 1$, where $\omega_c = eB/m^*$ is the cyclotron frequency, $m^* = 0.067 m_e$ is the effective mass of the charge carrier, m_e is the mass of an electron, e is the electron charge, and τ_q is the quantum lifetime. We can determine a characteristic B field B_q of 33 mT from the condition $\omega_c \tau_q = 1$ using the value of $\tau_q = 11.5$ ps extracted from analysis of the SdH oscillations in Appendix A, i.e., $B_q = m^*/e\tau_q$ [see also Fig. 9(a)], and note that weak SdH oscillations are still visible below B_q as represented by the red colored region

with diminished shading in Fig. 2(f)]. With increasing I_{DC}, the SdH oscillation amplitude first decays before the maxima and minima of the SdH oscillations invert, an effect called phase inversion (see Appendix A for discussion). Examples of inverted and noninverted SdH oscillations are given in Fig. 2(b). See also Fig. 10 where inversion occurs at a DC current $I_{PhI} \sim 0.2$ μA near 0.2 T.

In the vicinity of $B = 0$ T, we observe pronounced nMR, see Figs. 2(a) and 2(e) and discussion in Appendix B. The magnetoresistance decays rapidly with increasing B field until a strong change of slope marks the nMR boundary. Assuming a purely ballistic regime, an abrupt change of slope is predicted [66] to occur when $W = 2r_c$, where $r_c = m^* v_F/eB = v_F/\omega_c$ is the cyclotron radius, with a corresponding B field B_W, and $v_F = 1.9 \times 10^7$ cm/s is the Fermi velocity. In our case, $W = 15$ μm. Figure 9(a) in Appendix A shows a resistance versus B-field trace at zero DC current. The change in slope is most rapid at ~ 10 mT. We take this field to be an estimate of B_W, and this reasonably gives $W \sim 15$ μm (as an upper bound). However, the observed change of slope at the boundary is not as abrupt as in the calculations in Ref. [66], which is a source of imprecision in the estimation of the location of the boundary. Furthermore, accounting for undercut during the wet etching step in the fabrication of the Hall bar, and sidewall depletion, we expect the *effective* electronic width of the Hall bar W_{eff} to be smaller than W. In Sec. V, from a detailed analysis of the HIROs, we determine $W_{eff} \sim 11$ μm, and the corresponding B field $B_{W_{eff}} \sim 14$ mT. Throughout the text we will be careful in our usage of W and W_{eff} and make clear when it is important to distinguish the difference. Note in Fig. 2(f) we have marked the nMR boundary with $B_{W_{eff}}$ rather than B_W. Also accompanying the nMR is a distinctive double-peak feature, clear in Figs. 2(c) and 2(e), that we ascribe to ballistic transport.

Also close to $B = 0$ T, we can identify modifications to the nMR and the double-peak feature with increasing DC current that point to a growing influence of hydrodynamics [depicted by region marked HYDRO with cross hatching of increasing weight in Fig. 2(f)], see Ref. [77]. In a purely hydrodynamic regime, the hydrodynamic contribution to ρ_{xx} is expected to be strongest at $B = 0$ T, and in order to reach the strong hydrodynamic regime, the electron-electron scattering length l_{ee} should be smaller than the width of the Hall bar. We show in Sec. IV A that l_{ee} decreases with increasing I_{DC}, and so the signatures of viscous transport are stronger at high I_{DC}. See also the ρ_{xx} versus I_{DC} trace at $B = 0$ T in Fig. 2(d), which displays an initial decrease in ρ_{xx} with DC current. This behavior resembles that observed in a 2D wire and attributed to the Gurzhi effect, i.e., Poiseuille flow in electron transport [30]. In Sec. IV we will also examine the DC-current induced hydrodynamic correction to the Hall resistivity near zero field.

Lastly, in the phase diagram, we can identify HIRO peaks that fan out from the origin [see also the section in Fig. 2(e) that shows the HIROs either side of the nMR region near zero field]. The boundary above which HIROs are observed is delimited by I_{HIRO} in Fig. 2(f), and tracks the DC current position of the first-order HIRO peak that is linear in B [see Eq. (6) and Fig. 6(a)]. Similar to SdH oscillations, the HIRO peak amplitude is in principal related to the quantum lifetime. However, we find in Sec. V that the quantum lifetime extracted from
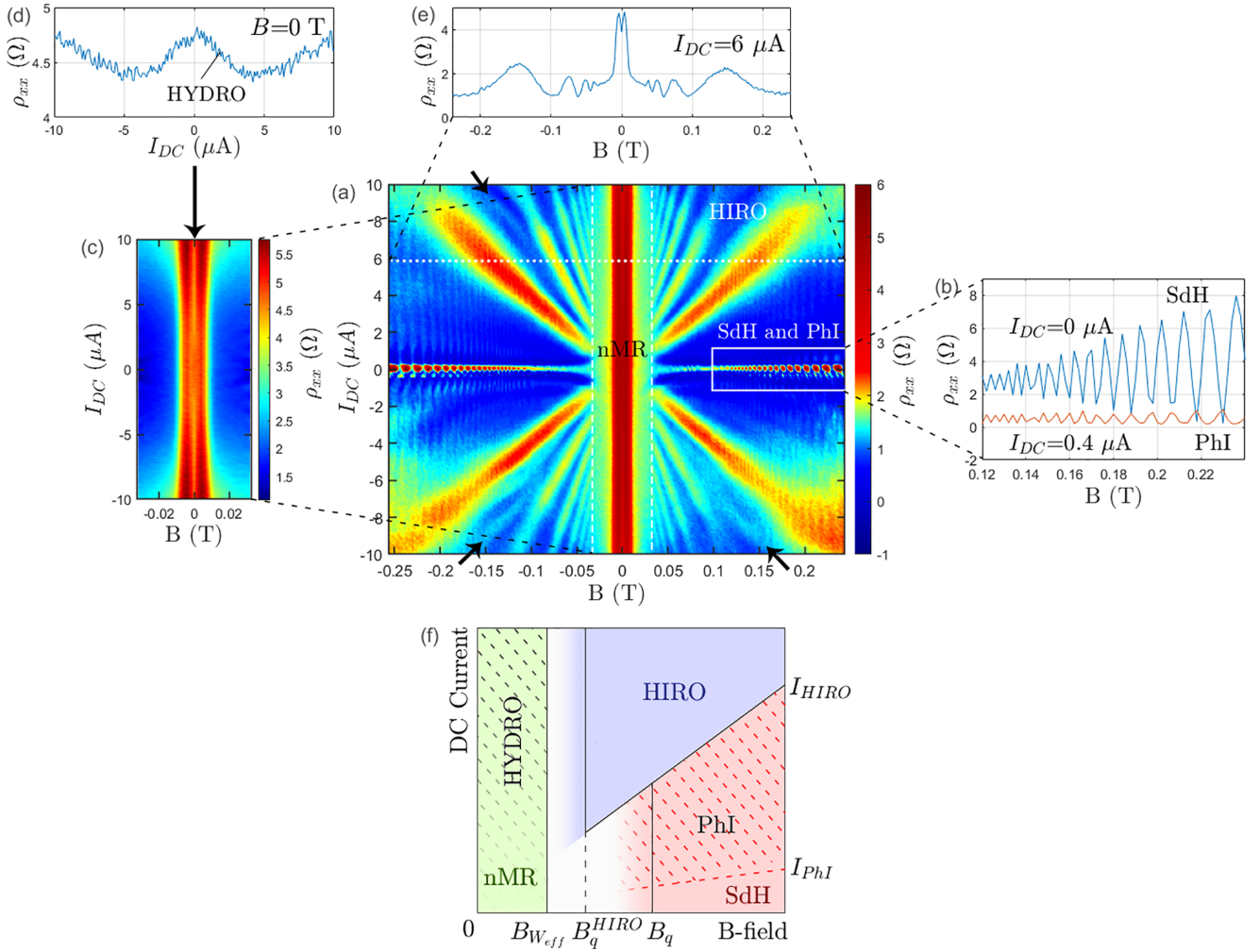
FIG. 2. (a) Map identifying the various phenomena ("phase diagram"). ρ_{xx} measured by sweeping the DC current and stepping the B field. A background parabolic dependence with I_{DC} and a small uniform linear dependence with B field are subtracted from the raw data to emphasize the features of interest in the phase diagram. The background I_{DC} dependence is discussed in Sec. IV A, and the small linear B dependence is likely due to inhomogeneity of the 2DEG material (the presence of a small density gradient can lead to a small Hall contribution to the magnetoresistance [75]). The Shubnikov-de Haas (SdH) oscillations and the accompanying phase inversion (PhI) of the SdH oscillations are visible close to zero DC current. The vertical band near $B = 0$ T identifies the negative magnetoresistance (nMR). The peaks forming a fan are the Hall-field induced resistance oscillations (HIROs). Black arrows in three of the four quadrants mark the "1.5" (HIRO-like) feature. (b) ρ_{xx} vs B sections at $I_{DC} = 0$ μA and $I_{DC} = 0.4$ μA showing respectively SdH oscillations and phase inverted SdH oscillations. (c) Expanded view of phase diagram around $B = 0$ T where nMR is observed. Note that here ρ_{xx} is plotted without removing the above mentioned background parabolic dependence with I_{DC} (see Sec. IV A). A double-peak feature is present on top of the nMR [see also panel (e)]. (d) ρ_{xx} vs I_{DC} trace at $B = 0$ T [marked by the vertical arrow in panel (c)]. The initial decrease in ρ_{xx} with current, i.e., negative differential resistivity, is a signature of hydrodynamics [30] (HYDRO). (e) ρ_{xx} vs B section taken at $I_{DC} = 6$ μA where we see the nMR and the double-peak feature around B = 0 T, and HIROs at higher B field. (f) Cartoon summarizing the regions identified in the upper-right quadrant of the phase diagram in panel (a). A more detailed description of the various phenomena, the boundaries between the phenomena, and certain marked characteristic B fields and DC currents can be found in the text.

the HIROs does not match the quantum lifetime extracted from the SdH oscillations. For this reason, the equivalent B field characterizing the onset of HIROs is marked separately as B_q^{HIRO} in Fig. 2(f). Note that weak HIROs are still visible below B_q^{HIRO} as represented by the blue colored region with diminished shading in Fig. 2(f)]. We can discern up to seven orders of HIRO peaks for a 10 μA DC current. Additionally, we observe unexpected HIRO-like features located between the first-order and the second-order HIRO peaks at high DC current, that are marked by black arrows in Fig. 2(a) [see also

Figs. 6(a) and 8], which we will refer to as the "1.5" features throughout this paper.

IV. HYDRODYNAMIC ELECTRON TRANSPORT

In this section we discuss the impact of hydrodynamics on electron transport when DC current is driven through the Hall bar. As discussed in the introduction, to reach the hydrodynamic regime, increasing the temperature is a common strategy taken to drive down l_{ee} so that the condition
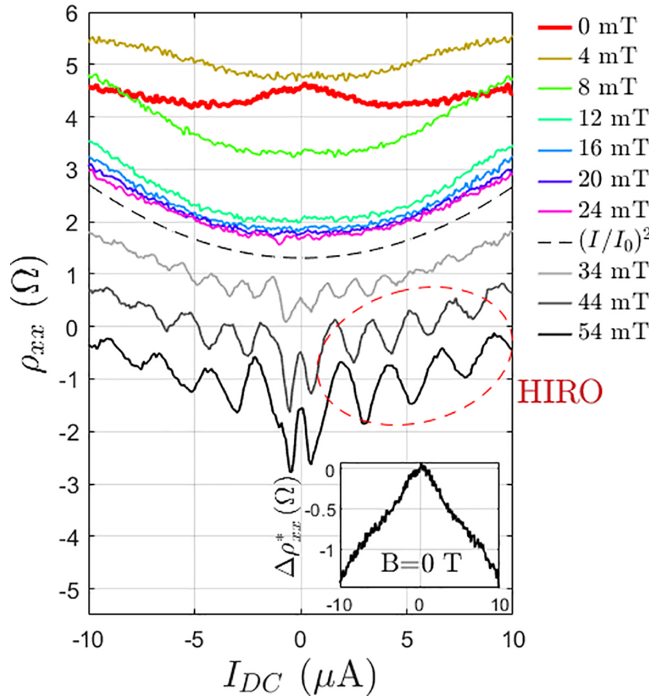
FIG. 3. ρ_{xx} vs I_{DC} for different B fields. The traces are taken from the data set shown in Fig. 2. Away from $B = 0$ T, ρ_{xx} exhibits a background quadratic dependence with respect to I_{DC}. The dashed line is a quadratic fit of the average ρ_{xx} from 12 mT to 24 mT, shifted down by 0.5 Ω for clarity. For this B-field range, hydrodynamic effects are suppressed, and SdH and HIRO are not yet observable. Above $B \sim 30$ mT, SdH oscillations and HIROs respectively start to appear at zero current and finite current, although the background quadratic dependence is still evident. Traces for $B > 30$ mT are shifted down progressively by 1 Ω for clarity. Red dashed line ellipse: HIRO amplitude decreases with increasing I_{DC} (see Sec. V for discussion). Inset: Hydrodynamic component $\Delta\rho_{xx}^* = \rho_{xx} - \rho_{xx,I=0} - \Delta\rho_{xx}^{bg}$ vs DC current in micro-amperes at $B = 0$ T. Here $\rho_{xx,I=0} \sim 4.6\,\Omega$. From a linear fit we find $\Delta\rho_{xx}^* = -0.155|I_{DC}|$). This component has a negative sign. See text for further discussion.

$l_{ee} \ll W$ is attained. We instead employ an increasing DC current to suppress l_{ee}, following the predictions by Giuliani and Quinn [27] that $l_{ee} \sim 1/I_{DC}^2$. We first demonstrate the DC current induced suppression of l_{ee}. Subsequently, we isolate the hydrodynamic contribution (correction) to both the differential longitudinal and transverse resistivities near $B = 0$ T, and compare to existing theories for hydrodynamic electron transport.

A. Current-induced suppression of electron-electron scattering mean free path

We start by discussing the necessary precondition for hydrodynamics, namely $l_{ee} \lesssim W$, and how by increasing the DC current flowing through the Hall bar device l_{ee} can be decreased. By careful inspection of vertical sections through the phase diagram in Fig. 2(a) near zero field, we can identify a general background quadratic dependence of ρ_{xx} with respect to I_{DC}, $\Delta\rho_{xx}^{bg}$. Other than at zero field, as illustrated in Fig. 3, this background quadratic dependence is clearly

seen for traces when $|B| \lesssim 30$ mT. At higher B field, the background quadratic dependence is still present but masked by the onset of SdH oscillations near zero current, and HIROs at finite current. From analysis of ρ_{xx} traces between 12 mT and 24 mT in Fig. 3, we find that the background quadratic dependence follows the relationship

$$\frac{\Delta\rho_{xx}^{bg}(I_{DC})}{\rho_{xx}(0)} = \left(\frac{I_{DC}}{I_0}\right)^2, \tag{1}$$

where $\rho_{xx}(0) = 1.81 \pm 0.01$ Ω, and $I_0 = 11.4 \pm 0.1$ μA. Strongly note that in our forthcoming discussion, $\Delta\rho_{xx}^{bg}$ is only a function of I_{DC}, i.e., for $|B| \lesssim 30$ mT it is assumed to have no B-field dependence, and furthermore, $\Delta\rho_{xx}^{bg}$ is defined to be zero at zero current. We attribute the quadratic dependence to a DC current induced increase of the electron-electron scattering rate τ_{ee}^{-1}. Generally, the resistivity of a 2DEG is proportional to the sum of the scattering rates from different sources namely $\rho_{xx} = (m^*/e^2 n) \sum_i \tau_i^{-1}$, where τ_i^{-1} are independent scattering rates for the different sources of scattering [78]. A DC current induced increase in the electron-electron scattering rate τ_{ee}^{-1} therefore results in a correction to the resistivity on the order of τ_{ee}^{-1} at low field.

In an ideal 2DEG, the following analytical expression for the evolution of the electron-electron scattering rate with DC current, rather than with temperature, was derived by Chaplik [79] and Giuliani and Quinn [27],

$$\tau_{ee}^{-1} = \frac{E_F}{4\pi\hbar}\left(\frac{\Delta}{E_F}\right)^2\left[\ln\left(\frac{E_F}{\Delta}\right) + \ln\left(\frac{2Q_{TF}}{k_F}\right) + \frac{1}{2}\right], \tag{2}$$

where Δ is the excitation (or excess) energy relative to E_F (satisfying $\Delta \ll \hbar^2 k_F Q_{TF}/m^*$), k_F is the Fermi wavevector, $Q_{TF} = 2m^*e^2/4\pi\epsilon_r\epsilon_0\hbar^2$ is the 2D Thomas-Fermi screening wave vector, ϵ_r is the dielectric constant ($\sim$13.1 for GaAs), and ϵ_0 is the vacuum permittivity. For a sufficiently small excess energy, Eq. (2) is approximately quadratic with respect to DC current. In our measurements, over the DC current range probed, the excess energy is small. The average resistance between 0 and 10 μA at zero field R_{av} is approximately 40 Ω, and so we estimate the maximum excess energy Δ to be of order $eV_{DC} \sim 0.4$ meV, where V_{DC} is the DC voltage drop between the two voltage probes along the Hall bar at 10 μA and B = 0 T. This estimated value of Δ satisfies the condition $\Delta \ll \hbar^2 k_F Q_{TF}/m^*$ since $\hbar^2 k_F Q_{TF}/m^* = 24.7$ meV. However, we note that the quantum interference experiment by Yacoby et al. [80] validating this theory suggested that Δ is proportional to eV_{DC} and the actual excess energy is smaller than the applied voltage [81].

As revealed in Fig. 3, in the narrow range around zero field ($|B| \lesssim 5$ mT), ρ_{xx} does not follow the I_{DC}^2 dependence. Specifically, at $B = 0$ T, ρ_{xx} decreases with I_{DC} before reaching a minimum at $\sim \pm 4$ μA, and then increases at higher DC current [also see Fig. 2(d)]. This behavior is reminiscent of that observed in an early study by Molenkamp and de Jong [30,32] in a wire formed from a 2DEG for which the decrease in the differential resistivity with increasing I_{DC} was assigned to a hydrodynamic effect. On subtracting the background quadratic dependence $\Delta\rho_{xx}^{bg}$ from ρ_{xx} at $B = 0$ T, relative to the zero current value of ρ_{xx}, we obtain the negative residual $\Delta\rho_{xx}^* = \rho_{xx} - \Delta\rho_{xx}^{bg}$, which exhibits a linear dependence in
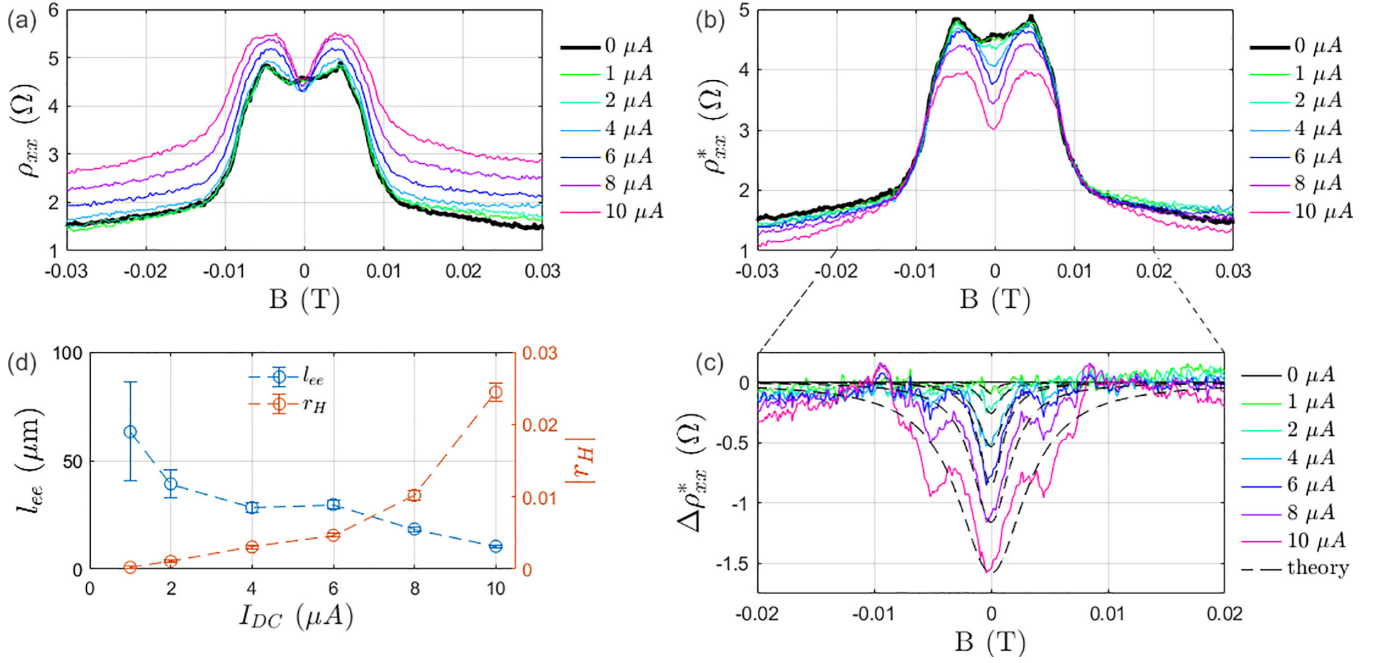
FIG. 4. (a) ρ_{xx} vs B traces on sweeping the B field for different DC currents (B-field sweep rate: 10 mT/min for zero current trace and 20 mT/min for all other traces). (b) $\rho_{xx}^* = \rho_{xx} - \Delta\rho_{xx}^{bg}$ vs B field. For each of the traces in (a) the background quadratic current dependence $\Delta\rho_{xx}^{bg}$ has been removed. For $|B| \lesssim 0.01$ T, we can see an increasingly strong decrease in ρ_{xx}^* on raising the DC current, which we attribute to hydrodynamics. (c) Solid lines: DC current-dependent deviation $\Delta\rho_{xx}^* = \rho_{xx}^* - \rho_{xx,I=0}^*$ of ρ_{xx}^* from the zero-current residual $\rho_{xx,I=0}^*$, namely the hydrodynamic component. Dashed lines: $r_H \Delta\rho_{xx}^{\mathrm{hyd}}$ fit to the data in a perturbative approach, where r_H is a fitting parameter reflecting the impact of the viscous correction, and $\Delta\rho_{xx}^{\mathrm{hyd}}$ is from the hydrodynamic theory as described by Eq. (3). For the fits, $W_{\mathrm{eff}} = 11$ μm is used. The distinct "dips" at $|B| \sim 5$ mT, and the weaker "dips" at $|B| \sim 8$ mT, are artifacts of the methodology due to the subtraction of the zero current trace, which has peaks at $|B| \sim 5$ mT and weak "shoulders" at $|B| \sim 8$ mT. Both constitute the double-peak feature, ballistic in origin, discussed in Appendix B, which itself has a DC current dependence. (d) l_{ee} and $|r_H|$ extracted from fits of the traces in (c) plotted against DC current. As I_{DC} increases, l_{ee} decreases and the hydrodynamic component ($|r_H|$) becomes stronger as expected.

DC current as shown in the inset to Fig. 3. In other words, ρ_{xx} versus DC current at $B = 0$ T is the sum of two components: a positive component $\Delta\rho_{xx}^{bg}$ quadratic in DC current related to the electron-electron scattering rate, and a negative component $\Delta\rho_{xx}^*$ linear in DC current. We attribute the latter to a DC current-induced hydrodynamic effect, driven by the enhancement of conductance of electrons in the hydrodynamic regime as expected in the ballistic regime [65,82], which leads to a negative hydrodynamic correction in the resistivity $\Delta\rho_{xx}^*$. We note that in contrast when hydrodynamics is induced by temperature in the nonballistic regime, a positive correction to the resistivity is expected as observed [51].

B. Hydrodynamic magnetoresistance

In the previous subsection, we established that increasing I_{ee} suppresses l_{ee}, a necessary precondition to enter the hydrodynamic regime. In this subsection, we analyze the evolution of ρ_{xx} with I_{DC} for small B fields ($|B| < 10$ mT), and compare the change in ρ_{xx} to that expected from existing hydrodynamic theory. Figure 4(a) shows ρ_{xx} versus B traces for different DC currents up to 10 μA. The goal is to first identify and then isolate the various components that can contribute to the DC current dependence of ρ_{xx}. One component, as established in the previous subsection (see Fig. 3), is the general background quadratic increase in ρ_{xx} with DC current $\Delta\rho_{xx}^{bg}$, and another component near zero field, the focus of our attention, that

we will argue is hydrodynamic in origin. By removing $\Delta\rho_{xx}^{bg}$ from ρ_{xx} over the B range from –30 mT to +30 mT, and examining the residual ρ_{xx}^* plotted in Fig. 4(b), we find that for $|B| \lesssim 10$ mT, there is clearly a growing negative component to ρ_{xx} with increasing DC current. We can isolate this negative component from the nMR and the double-peak feature by computing $\Delta\rho_{xx}^* = \rho_{xx}^* - \rho_{xx,I=0}^*$, the DC current-dependent deviation of ρ_{xx}^* from the zero-current residual $\rho_{xx,I=0}^*$. The deviation is plotted in Fig. 4(c). We attribute this deviation to hydrodynamics because of its growing amplitude with increasing DC current, and decreasing amplitude with increasing B field. The latter is discussed in Ref. [66]. Next, we discuss our method to compare $\Delta\rho_{xx}^*$ to existing theory.

We now examine in further detail the experimental data in Fig. 4(c). In the purely hydrodynamic regime, following Scaffidi *et al.* [66], the viscous correction to the magnetoresistance for a 2DEG when $l_{ee} \ll W \ll l_{mfp}$ can be expressed as

$$\Delta\rho_{xx}^{\mathrm{hyd}} = \frac{m^*}{e^2 n} \frac{v_F l_{ee}}{W^2} \frac{3}{1 + \left(\frac{2l_{ee}}{r_c}\right)^2}. \quad (3)$$

For our Hall bar device, $W_{\mathrm{eff}} \sim W \ll l_{mfp}$ is trivially satisfied since $l_{mfp} = 145$ μm. Using Eq. (2) with $\Delta = eV_{\mathrm{DC}} = eI_{\mathrm{DC}}R_{av}$, $l_{ee} = v_F \cdot \tau_{ee}$ is predicted to be smaller than W for $I_{\mathrm{DC}} \gtrsim 9.5$ μA. Therefore, for an increasing DC current up to 10 μA, the maximum applied, the 2DEG transitions from the ballistic regime ($W \ll l_{ee}, l_{mfp}$) to the hydrodynamic regime

[77]. This transitional phase has *both* ballistic and hydro-dynamic contributions. To describe this regime we use a perturbative approach, where we assume that (i) the 2DEG is initially in the ballistic regime, (ii) the change in ρ_{xx} with increasing DC current near zero field is solely hydrodynamic in origin, and (iii) the change is proportional to the viscous correction described in Eq. (3). In other words, the change in ρ_{xx} with increasing DC current following our model has the form

$$\Delta\rho_{xx} = \rho_{xx} - \rho_{xx,I=0} = \Delta\rho_{xx}^{bg} + r_H\Delta\rho_{xx}^{hyd}, \qquad (4)$$

where r_H is a dimensionless parameter characterising the relative strength of the viscous correction at different DC currents. The term $r_H\Delta\rho_{xx}^{hyd}$ in Eq. (4) corresponds to $\Delta\rho_{xx}^*$ determined from the experimental data and plotted in Fig. 4(c). Fitting $r_H\Delta\rho_{xx}^{hyd}$ to $\Delta\rho_{xx}^*$, we can extract values for both l_{ee} and r_H. The obtained DC current dependencies of l_{ee} and r_H are presented in Fig. 4(d). l_{ee} is found to decrease with increasing DC current, and its value is comparable to that calculated from theory Eq. (2) [for example, at 10 μA, Eq. (2) predicts $l_{ee} = 14$ μm and we obtain $l_{ee} \sim 11$ μm], which supports our hydrodynamic interpretation in the small B-field regime. $|r_H|$ increases faster than linear with DC current, which is reflective of the growing hydrodynamic component. Lastly, we estimate the electron shear viscosity [26], defined as $\eta = v_F^2\tau_{ee}/4$, to be 0.7 m²/s at 10 μA. In comparison, in the work of Gusev *et al.* in Ref. [51] for which hydrodynamics is temperature-induced and no DC current is applied, η is found to be 0.3 m²/s at T = 1.4 K.

Comparing our experimental observations for DC current-induced hydrodynamics in the differential longitudinal resistivity in Fig. 4(a) with those for temperature-induced hydrodynamics in recent works of Gusev *et al.* [51] and Raichev *et al.* [71] there is one notable difference. In our case, the "dip" at zero field is seen to grow with increased DC current. In the case of Gusev *et al.* and Raichev *et al.*, the "dip" is seen to weaken with increased temperature, and by 40 K the low-field double-peak feature has disappeared (a single peak showing nMR remains). In the work of Raichev *et al.*, a classical kinetic model was used to compute the joint ballistic and hydrodynamic contributions for temperature-induced hydrodynamics. In the theoretical analysis the authors assume that boundary scattering is independent of temperature, which is reasonable in their experiments. However, this is likely not true for our case where we increase the DC current, which will lead to a change of the effective edge potential due to the large bias along the edges of the HB. Indeed, a large current is expected to lead to less diffusivity in boundary scattering, due to the averaging over a wide energy window, and hence to an enhanced double-peak feature as observed in Fig. 4(a).

C. Hydrodynamic contribution to Hall resistivity

In the previous subsection, we discussed the growing hydrodynamic contribution to ρ_{xx} with increasing I_{DC} near zero field. Similarly, hydrodynamics affects ρ_{xy}. In Fig. 5(a), we show the DC current-dependent deviation of ρ_{xy} from the conventional (bulk) Hall resistivity ρ_{xy}^{bulk}, namely $\Delta\rho_{xy} = \rho_{xy} - \rho_{xy}^{bulk}$, for I_{DC} values of 0, 4, and 8 μA, where $\rho_{xy}^{bulk} = -B/en$. At B = 0 T, the sign of the slope changes from
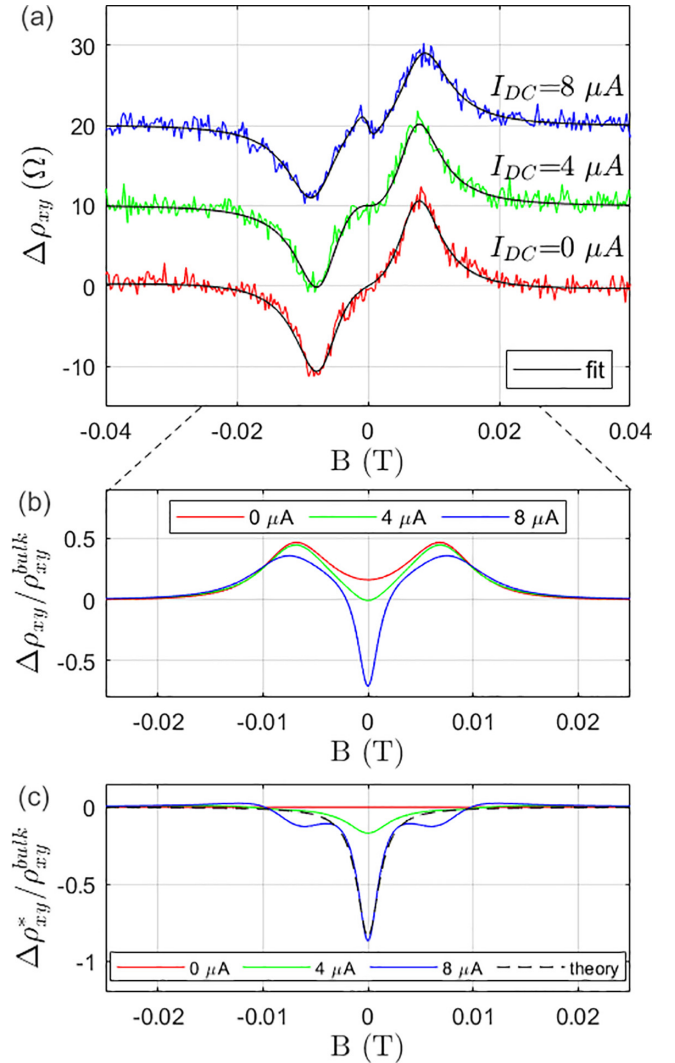

FIG. 5. (a) Deviation from the conventional (bulk) Hall resistivity $\Delta\rho_{xy} = \rho_{xy} - \rho_{xy}^{bulk}$ for three values of DC current. The plots are derived from ρ_{xy} vs B traces on sweeping the B field at 20 mT/min. The black lines are fits to a sum of polynomials that allow accurate division by ρ_{xy}^{bulk}. Plots are offset by 10 Ω for clarity. The change in the slope at zero field from positive to negative with increasing DC current is a signature of the growing influence of hydrodynamics. The extrema near $|B| \sim 8$ mT arise from ballistic transport [51,71,83]. We note that the derivative of the ρ_{xx} trace for $I_{DC} = 8$ μA has a close resemblance to the $\Delta\rho_{xy}$ trace for $I_{DC} = 8$ μA. (b) Calculated from the fits in panel (a), the ratio $\Delta\rho_{xy}/\rho_{xy}^{bulk}$ is plotted to emphasize the hydrodynamic component near 0 T. The negative value near 0 T in the 8 μA curve is a clear sign of hydrodynamics. (c) Isolated hydrodynamic component $\Delta\rho_{xy}^*/\rho_{xy}^{bulk} = (\Delta\rho_{xy} - \Delta\rho_{xy,I=0})/\rho_{xy}^{bulk}$ determined from curves in panel (b). Dashed line: Fit to $I_{DC} = 8$ μA curve following hydrodynamic theory Eq. (5); see text for parameters. For the fit, $W_{eff} = 11$ μm is used.

positive to negative with increasing DC current. Other than a global sign difference, note that the form of the $I_{DC} = 8$ μA trace is similar to traces reported in Ref. [51] measured between 1.7 K and 40 K with zero DC current supporting our hydrodynamic interpretation. Following the approach of Gusev *et al.* where the induced change with temperature

was tracked instead [51], the induced change with DC current we see can be better visualized by examining the ratio $\Delta\rho_{xy}/\rho_{xy}^{\text{bulk}}$: see Fig. 5(b). As with ρ_{xx}, we analyze the change in ρ_{xy} with DC current near the 0 T and compare to theory in a perturbative method. In the purely hydrodynamic regime, incorporating earlier work by Alekseev [64], the viscous Hall correction to ρ_{xy} was derived by Scaffidi *et al.* [66] and found to be

$$\frac{\Delta\rho_{xy}^{\text{hyd}}}{\rho_{xy}^{\text{bulk}}} = \left[-\frac{6}{1 + (2l_{ee}/r_c)^2} \left(\frac{l_{ee}}{W}\right)^2 \right], \quad (5)$$

where $\Delta\rho_{xy}^{\text{hyd}} = \rho_{xy} - \rho_{xy}^{\text{bulk}}$ is the hydrodynamic contribution to the bulk Hall resistivity. Following the same approach as for ρ_{xx}, the change in the deviation of ρ_{xy} with increasing DC current relative to the zero current deviation $\Delta\rho_{xy}^* = \Delta\rho_{xy} - \Delta\rho_{xy,I=0}$ corresponds to $r_H\Delta\rho_{xy}^{\text{hyd}}$ in a perturbative method, where r_H is a dimensionless fitting parameter reflecting the impact of the viscous correction to ρ_{xy} at different DC currents. In Fig. 5(c), $\Delta\rho_{xy}^*/\rho_{xy}^{\text{bulk}} = (\Delta\rho_{xy} - \Delta\rho_{xy,I=0})/\rho_{xy}^{\text{bulk}}$ is plotted, and we find that increasing the DC current "amplifies" the minimum at zero field. The 8 µA curve is fitted to $r_H\Delta\rho_{xy}^{\text{hyd}}/\rho_{xy}^{\text{bulk}}$. We find the minimum value at 0 T equates to a l_{ee} of 29 µm, with a r_H factor of 0.019. These values are consistent with those from our earlier analysis of ρ_{xx} and theory Eq. (2) for l_{ee} [see also Fig. 4(d)].

Echoing our commentary at the end of the previous subsection, comparing our experimental observations for DC current-induced hydrodynamics in the differential transverse resistivity in Fig. 5(a) with those for temperature-induced hydrodynamics in recent works of Gusev *et al.* [51] and Raichev *et al.* [71] there is again a notable difference. In our case, the change in sign of the slope at zero field occurs on increasing the DC current (which increases the electron temperature but not the bath temperature). In the case of of Gusev *et al.* and Raichev *et al.*, the distinctive line shape is seen to weaken with increased temperature, and by 40 K the deviation from the bulk Hall resistivity is small. High temperature also leads to both an increase in the phonon population and decrease decrease of the mobility.

V. HALL-FIELD INDUCED RESISTANCE OSCILLATIONS

So far, in the phase diagram, we have described in detail the SdH oscillations and the accompanying PhI of the SdH oscillations located near zero current, and the nMR and the effects of DC current-induced hydrodynamics near zero field. Away from both $B = 0$ T and $I_{\text{DC}} = 0$ µA we observe HIROs. In Fig. 2(a), HIRO peaks up to the seventh order that fan out from the origin are identifiable. HIROs were first reported by Yang *et al.* [5], and have since been studied extensively both experimentally [6–19] and theoretically [3,4,84–87]. HIROs emerge in the weak field magnetoresistance in high mobility 2DEGs due to resonant electron transitions between LLs that are spatially tilted along the direction of the transverse electric (Hall) field when DC current is passed along the Hall bar. In the original work by Yang *et al.* [5], it was explained that Zener tunneling can occur when the electron hopping distance ΔY_M between different Landau levels is equal to γr_c, where $\Delta Y_M = M\hbar\omega_c/eE_H$, M is an integer, E_H is the Hall field,

and $\gamma \approx 2$ according to theory. This leads to HIRO maxima in $\partial\rho_{xx}/\partial|B|$ with position in the $I_{\text{DC}} - B$ plane obeying the condition

$$B = \gamma\frac{\sqrt{2\pi}m^*}{e^2\sqrt{n}}\frac{I_{\text{DC}}}{WM}. \quad (6)$$

For the regime $k_BT \gg \hbar\omega_c$, where SdH oscillations are smeared out by temperature, Vavilov *et al.* [86], found that the HIROs in the differential resistivity can be approximately described by the expression

$$\rho_{xx,\text{HIRO}} \approx \frac{16m^*}{\pi e^2 n\tau_\pi}\exp\left(-2\frac{\pi}{\omega_c\tau_q}\right)\cos\left(2\pi\frac{2I_{\text{DC}}k_F}{enW\omega_c}\right), \quad (7)$$

where τ_π is the backscattering lifetime. In the derivation [86], the oscillatory dependence of the differential resistivity stems from the product of the oscillatory DOS and the oscillatory nonequilibrium distribution function. When integrated over the nonequilibrium energy range, the remaining leading oscillatory term is squared, which explains the additional factor of two in the exponential damping factor $\exp(-2\pi/\omega_c\tau_q)$ in Eq. (7) as compared to the SdH oscillation damping factor in Ando's expression in Eq. (A1). The amplitude of the induced oscillation according to Eq. (7) is proportional to the backscattering rate $\sim\tau_\pi^{-1}$, which is related to sharp disorder enabling a "kick" from one cyclotron orbit into another. The full theory by Vavilov *et al.* also takes into account effects at relatively low current $(2\pi I_{\text{DC}}k_F/enW\omega_c < 1)$ due to variation of the occupation factors for the electronic states. We now compare the experimental data to the theories in Refs. [5,86], report the extracted fitting parameters, and discuss other relevant observations and implications.

We first analyze our experimental HIRO data with the model of Yang *et al.* [5]. We extract the HIRO maxima in the derivative of the differential resistivity $\partial\rho_{xx}/\partial|B|$ and compare with the expression in Eq. (6). The positions of the HIRO maxima for peaks up to the sixth order are plotted in Fig. 6(a). The position of the maxima can be collapsed onto a single line, essentially the line tracking the first-order HIRO peak, following the relation $B \cdot M \propto I_{\text{DC}}/W$. With $W = 15$ µm, the slope of the single line in Fig. 6(b) is found to be 324 mT/(A/m), and from Eq. (6), we obtain $\gamma = 2.4$. This result is consistent with the theoretical value of $\gamma \approx 2.0$ reported in the work of Yang *et al.* [5], and their empirically determined γ values (1.7–2.1) for Hall bars with a 2DEG density close to that for our Hall bar device. Note that had we used $W_{\text{eff}} \sim 11$ µm to calculate the nominal current density, we would obtain $\gamma = 2.1$.

In the model of Vavilov *et al.* [86], the amplitude of the HIROs depends on τ_π and τ_q, respectively the backscattering and quantum lifetimes. We fit ρ_{xx} versus B sections with Eq. (7) to obtain τ_π, τ_q, and additionally W_{eff}. Note that rather than assume W is fixed and equal to the nominal lithographic width of the Hall bar, W is treated as a fitting parameter, which we call W_{eff}. Furthermore, we choose to fit $\partial\rho_{xx}/\partial B$ [see Fig. 7(a)], essentially the partial derivative of Eq. (7) with respect to B, instead of ρ_{xx}, to remove the aforementioned background linear B dependence in the data, and to reduce fitting errors, although fits to either are equivalent and give nearly identical fitting parameters. Parameters τ_q and W_{eff}
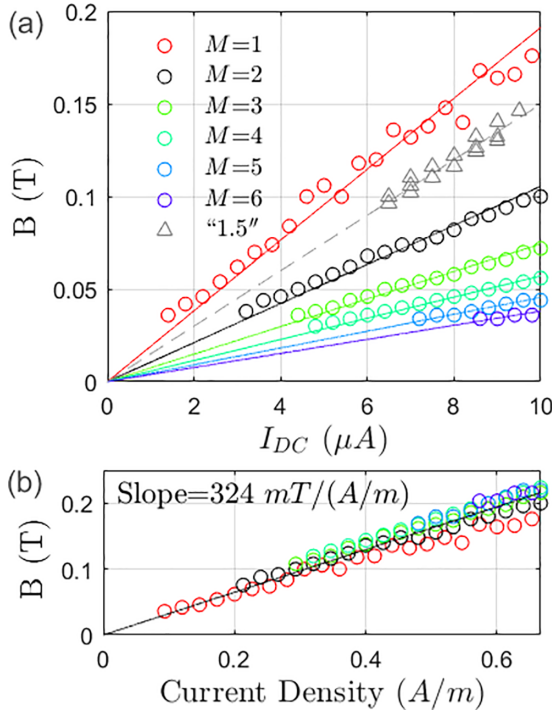
FIG. 6. (a) Fan diagram of HIRO maxima in $\partial\rho_{xx}/\partial|B|$ for each peak up to the sixth order. Points are extracted from the Fig. 2(a) data set for HIROs in the +I and +B quadrant. Triangles: Maxima in $\partial\rho_{xx}/\partial|B|$ of the "1.5" features visible in three of the four quadrants in Fig. 2(a) (the "1.5" feature in the +I and +B quadrant is not visible). Dashed line corresponds to (effective) M = 1.44. (b) All HIRO maxima collapse on to a single line following the relation $B.M \propto I_{DC}/W$. The slope is used to extract the parameter γ. In panel (b) we have used W = 15 μm rather than W_{eff} to calculate the nominal current density so the value of the slope can be compared to those in the literature.

obtained are presented in Fig. 7(b). τ_q is discussed more extensively in the following paragraph. The effective electronic width W_{eff} is found to be ∼11 μm over the full 10 μA current range. Parameter W_{eff} is obtained from the HIRO frequency and is extremely accurate as in Eq. (7) it is independent of the amplitude of the HIROs. The effective electronic width is smaller than the lithographic width of the Hall bar W = 15 μm. As commented on earlier, we attribute the difference to a combination of undercut during the wet etching step in the fabrication of the Hall bar, and sidewall depletion. For the backscattering lifetime, we obtained $\tau_\pi \approx 5$ ns with no significant current dependence. We note that the corresponding scattering length associated with the backscattering process is $l_\pi = v_F \tau_\pi \simeq 1$ mm. This length scale is much larger than our Hall bar device size and therefore cannot be interpreted as the typical distance between backscattering impurities.

The values of the quantum lifetime extracted from HIROs in Fig. 7(b) are notable for two reasons. First, τ_q decreases with increasing DC current, and second, τ_q here far exceeds the value of $\tau_q = 11.5$ ps extracted earlier from the SdH oscillations [see Fig. 9]. Concerning the first point, in the model of Vavilov *et al.* [86], the HIROs amplitude does not depend on DC current, whereas our data shows that the

amplitude of the HIROs decreases with increasing DC current [see red dashed line ellipse in Fig. 3]. This decrease was also observed in another experiment featuring a 2DEG in a MgZnO/ZnO heterostructure [17], and was attributed to enhanced electron-electron scattering with increasing electron temperature. The relationship $1/\tau_q \propto I_{\mathrm{DC}}^2$ was found. Using the same analysis for our Hall bar, we obtain $\tau_q(0)/\tau_q(I_{\mathrm{DC}}) = 1 + (I_{\mathrm{DC}}/I_0)^2$ where (the extrapolated zero current quantum lifetime) $\tau_q(0) = 41.2 \pm 0.7$ ps, and $I_0 = 8.66 \pm 0.04$ μA [see fit in Fig. 7(b)]. The value of I_0 here is comparable to that obtained from the background quadratic dependence to ρ_{xx} discussed in Sec. IV A relating to Eq. (1). Concerning the second point, the extracted value of τ_q from fitting HIROs, which we now explicitly identify as τ_q^{HIRO}, varies from ∼40 ps at 2 μA to ∼18 ps at 10 μA, whereas the extracted value of τ_q from fitting the SdH oscillations *at zero DC current*, also now explicitly identified as τ_q^{SdH}, is ∼11 ps. An alternative method presented in Refs. [9,18,88] to extract the exponential damping of SdH oscillations and HIROs is to plot the logarithm of the SdH oscillation and HIRO extrema amplitudes as a function of inverse B field as shown in Fig. 7(c). The slope of the plots corresponds to $-\zeta\pi/\mu_q$, where $\mu_q = e\tau_q/m^*$ is the quantum mobility. From Eqs. (A1) and (7) we expect $\zeta = 1$ for the SdH oscillations and $\zeta = 2$ for the HIROs, i.e., based on these equations the slope for HIROs should be twice the slope for the SdH oscillations. However, this is clearly not the case as can be seen in Fig. 7(c). For example, for the 5 μA data, the slope for the HIROs is in fact even less than the slope for the SdH oscillations (consistent with the observation that the value for τ_q^{HIRO} is a factor of two to four times larger than the value for τ_q^{SdH}). Note that the values obtained for the quantum lifetime do not depend significantly on the methods used [when we compare the value of τ_q^{SdH} obtained from the full fit method in Fig. 9(b) with that from the fit for the alternative method in Fig. 7(c), 11.5 ps versus 11 ps, and likewise the value of τ_q^{HIRO} obtained from the full fit method in Fig. 7(a) with that from the fit for the alternative method in Fig. 7(c), 31 ps versus 29 ps both for 5 μA current], i.e., both methods lead to very similar values. Examining closely the theory in Ref. [86], it is assumed that the quantum lifetime for SdH oscillations and HIROs are the same. Furthermore, in the derivation of Eq. (7) it is also assumed that $k_B T \gg \hbar\omega_c$. This equates to a temperature exceeding 0.5 K at 25 mT, which clearly does not hold for our experimental situation. This may explain the observed discrepancy between τ_q^{SdH} and τ_q^{HIRO}, and suggests that a theory for HIROs extended to the low-temperature regime is needed in order to correctly explain the observed amplitude of the HIROs. It is likely that at low temperature, when temperature smearing is small, the amplitude of the HIROs is proportional to the oscillatory DOS and not its square as in the derivation of Eq. (7) that assumes $k_B T \gg \hbar\omega_c$. We stress that the quantum lifetime is normally determined from the SdH oscillations (τ_q^{SdH}) *at zero DC current*. Inferring this quantum lifetime is the same as the quantum lifetime determined solely from measurement of HIROs (τ_q^{HIRO}), a nonlinear transport phenomenon observed at finite DC current, therefore has to be done with caution [18].

Lastly, we observe unexpected HIRO-like features located between the first-order and the second-order HIRO peaks at
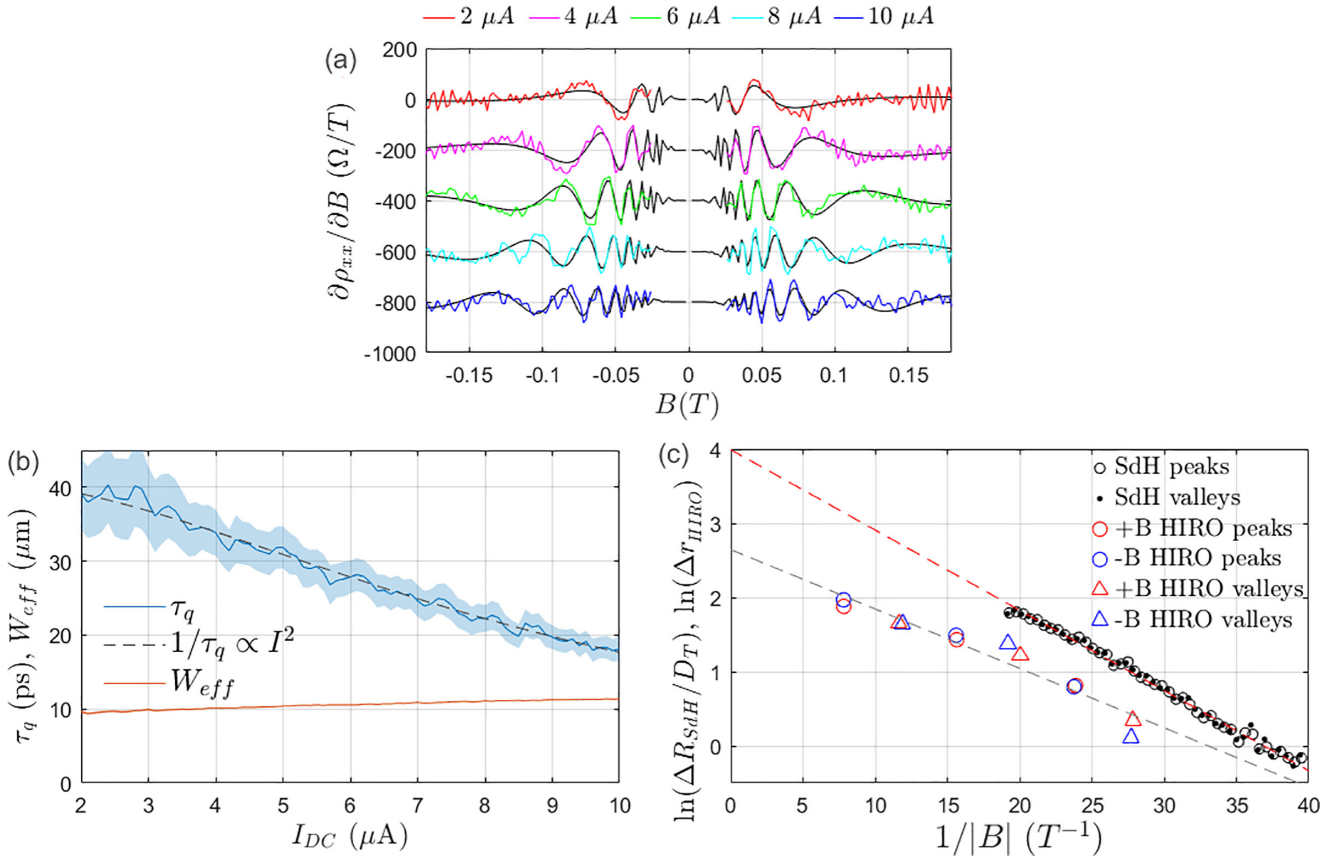
FIG. 7. (a) $\partial\rho_{xx}/\partial B$ vs B for selected DC currents. ρ_{xx} data are from sections through the map in Fig. 2(a). Black lines: fits to data with derivative of Eq. (7). The plots are offset by 200 Ω/T for clarity. (b) HIRO parameters τ_q and W_{eff} obtained from fitting $\partial\rho_{xx}/\partial B$ vs B sections for positive I_{DC}. Dashed line: $1/\tau_q \propto I_{DC}^2$ fit to τ_q values. (c) Log plot vs 1/B of SdH oscillation peak and valley amplitudes in r_{xx} at $I_{DC} = 0$ μA, ΔR_{SdH}, and HIRO peak and valley amplitudes in r_{xx} at $I_{DC} = 5$ μA, Δr_{HIRO}. We use both positive and negative B-field extrema for the HIRO data points. For HIROs, the 5 μA section is selected for analysis because for this current there are a sufficient number of resolved extrema to analyze, and the "1.5" feature that could influence the minimum between the first- and second-order peaks has not yet developed. Red dashed line for SdH oscillations: fit with Eq. (A1) where D_T is the thermal damping factor, and τ_q^{SdH} is determined from the slope (τ_q^{SdH} = 11 ps). Gray dashed line for HIROs: fit with Eq. (7) where τ_q^{HIRO} at 5 μA is determined from the slope (τ_q^{HIRO} = 29 ps).

high DC current. These features are marked by black arrows in Fig. 2(a) in three of the four quadrants, and appear for a DC current exceeding 6 μA and a B field above 0.1 T [see
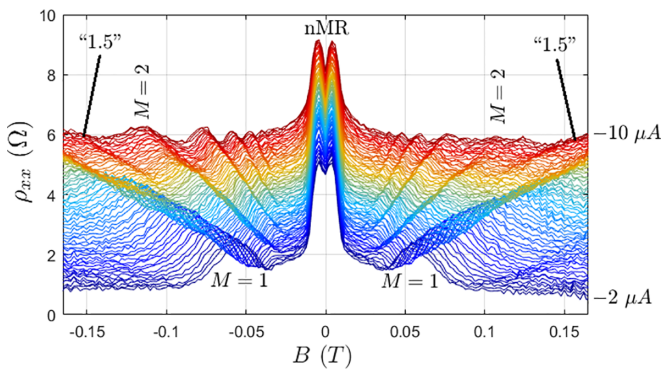

FIG. 8. ρ_{xx} vs B sections through the map in Fig. 2 (a) for negative DC currents between −2 μA and −10 μA. Plots are offset from each other by +0.06 Ω for clarity. The $I_{DC} = −2$ μA plot has no offset. The plots are arranged to emphasize the emergence of the "1.5" features at high current.

Fig. 6(a), and also Fig. 8]. Although not expected in the standard picture of HIROs, these features are HIRO-like in the sense that they lie on a line following the relation $B \propto I_{DC}$ and appear as part of the fan formed from the expected HIRO maxima (M=1, 2, 3,...). We have referred to them as "1.5" features since their *effective* index $M \sim 1.5$. We do not claim M is quantized at 3/2: specifically from the fit in Fig. 6(a) we determine $M = 1.44 \pm 0.04$. Currently we have no clear understanding of the origin of the "1.5" feature, but speculate that it may be related to the lifting of the spin degeneracy, which is observed in the Hall bar measured in the SdH oscillations at a similar B field (∼0.15 T: data not shown). We note that Hatke *et al.* [89] interestingly reported a HIRO-like feature at $M = 0.5$, also referred to as fractional HIRO in Ref. [3]; however, this was observed in a measurement performed under microwave illumination. We stress that we have observed the "1.5" features with no microwaves applied.

VI. CONCLUSIONS

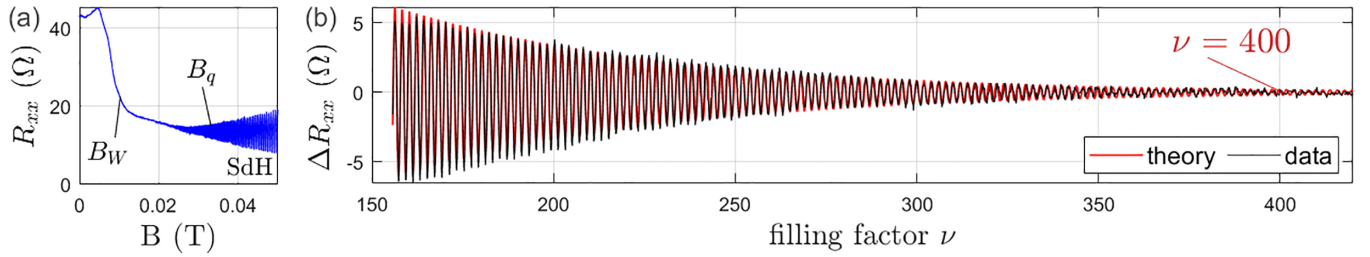In conclusion, for an ultrahigh mobility 2DEG in a narrow Hall bar we measured ρ_{xx} as a function of B field and DC

FIG. 9. (a) Resistance R_{xx} vs B trace. Here R_{xx} is taken to be r_{xx} at $I_{DC} = 0\,\mu A$, and for this particular measurement where the B field is swept at 1 mT/min the AC excitation current is 40 nA. At low B field, there is strong negative magnetoresistance up to field $B_W \sim 10$ mT as discussed in Sec. III and in Appendix B. $B_q = 33$ mT is related to τ_q and is defined in Sec. III. (b) SdH oscillation amplitude ΔR_{xx} determined from panel (a) plotted vs filling factor ($\nu \propto 1/B$). The black line is the data, fitted to Eq. (A1), red line, with obtained parameters $n = 2.0 \times 10^{11}\,cm^{-2}$, $R_0 = 11.4 \pm 0.6\,\Omega$, and $\tau_q = 11.5 \pm 0.3$ ps. $\nu = 400$ corresponds to B = 21 mT.

current at the base temperature of a dilution refrigerator. This measurement approach provides in a single 2D map a "global" view of different low-magnetic-field nonlinear phenomena in a 2DEG. We identified and analyzed several different phenomena (and the boundaries between these phenomena): SdH oscillations, PhI of the SdH oscillations, nMR, a double-peak feature, and HIROs. By analyzing the data with existing theories, we extracted relevant parameters as summarized in Table II. For the SdH oscillations, we found that the Ando formula in combined with an electron heating model can explain both the initial decrease in the SdH oscillation amplitude and then the subsequent PhI of the SdH oscillations with increasing DC current (Appendix A). As the zero-field resistance is largely determined by the nMR in our narrow Hall bar, we found that a fit of the SdH oscillations was essential to determine the appropriate resistance (R_0) needed to estimate the mobility (Appendix A). We confirmed that the nMR can be explained purely as a ballistic effect with a numerical simulation (Appendix B). From fits of the HIROs, we extracted the effective electronic width of the Hall bar $W_{eff} \sim 11\,\mu m$. We also found that the quantum lifetime determined from analysis of the SdH oscillations at zero DC current τ_q^{SdH} does not match the quantum lifetime determined from analysis of the HIROs at finite DC current τ_q^{HIRO}. The factor of two to four difference deserves further attention and would suggest a more careful theoretical treatment of HIROs at low temperature is needed. This also implies that HIROs, which is a nonlinear effect, cannot be used in a direct way to infer the quantum lifetime in the linear regime (from SdH oscillations). Unexpectedly, a HIRO-like feature nestled between the first- and second-order HIRO maxima was observed with an effective index $M = 1.44 \pm 0.04$. The origin of this feature is not understood at present.

A major part of our paper has demonstrated the growing influence of hydrodynamics brought about by applying a DC

current, rather than changing the temperature as more commonly employed [77,90,91], to reduce the electron-electron scattering length l_{ee} to the point that this length becomes comparable to or even smaller than W_{eff}. For a DC current of $\sim 10\,\mu A$, we determined $l_{ee} \sim W_{eff} \sim 11\,\mu m$. DC current-induced hydrodynamics complements temperature-induced hydrodynamics [90]. The current-induced case is a nonlinear process, where the electron distribution is pushed strongly out of equilibrium, while in the temperature-induced case the electron distribution is thermal (and transport is linear), but it also increases the population of phonons [91], which reduces the carrier mobility and eventually suppresses hydrodynamic behavior. From a detailed analysis of the data within a −10 mT to +10 mT window, we isolated the growing hydrodynamic contribution to both the differential longitudinal and transverse (Hall) resistivities with increasing DC current. For the former (latter) the signature was found to be a growing "dip" (a change in sign of the slope) at zero field. We quantified the hydrodynamic corrections using a perturbative method. In theoretical works such as those in Refs. [66,71], the magnetoresistance in the hydrodynamic and ballistic regimes is modelled for linear transport, whereas a full model that incorporates nonlinear transport relevant to our experimental situation merits investigation.

We stress that the 2D phase diagram we measured for an ultrahigh mobility 2DEG offers more than just a means to investigate the constituent transport regimes in isolation. The global view looking at *all* the transport regimes *together* has provide new information and perspective. For example, the nMR and hydrodynamic regimes occupy the same region in the phase diagram and so the nMR must be considered when analyzing the hydrodynamic component; the electron temperature estimated from SdH and PhI is relevant to the discussion of the hydrodynamic regime; quantities such as the quantum lifetime extracted from SdH and HIROs regimes, presumed to be the same, are found to be significantly different; and a high-resolution phase diagram can show features such as the "1.5" feature in the HIROs regime that would be easy to miss if only a limited number of data traces were taken.

In the measurements described, the maximum DC current applied was limited to 10 μA and the temperature was fixed at the base temperature of the dilution refrigerator. Higher DC current and higher temperature could enhance further hydrodynamic corrections and bring other phenomena in to play [91]. Measurement of differential resistivity maps as we have

TABLE II. Summary of key extracted parameters. The values of l_{ee} and η are for $I_{DC} = 10\,\mu A$ determined in Sec. IV. τ_q^{HIRO} depends on I_{DC} hence a range of values is given (see Sec. V).

W_{eff} (μm)	l_{ee} (μm)	η (m^2/s)	τ_q^{SdH} (ps)	τ_q^{HIRO} (ps)	τ_π (ns)
11	11	0.7	11.5	18–40	5

demonstrated here at low magnetic field is a powerful and convenient approach to probe numerous phenomena. We also draw attention to a recently published and complementary paper on hydrodynamic transport in a GaAs/AlGaAs ultrahigh mobility 2DEG although the DC current dependence and Hall resistivity were not investigated [92].

ACKNOWLEDGMENTS

APPENDIX A: SHUBNIKOV-DE HAAS OSCILLATIONS AND PHASE INVERSION

SdH oscillations arise from B-field induced LLs and the oscillating density-of-states (DOS) at the Fermi level [93–96]. For an extensive review of SdH oscillations see Ref. [3]. In the small B-field regime the SdH oscillations in the resistance $R_{xx} = V_{xx}/I$ (which is equivalent to r_{xx} in the limit of zero DC current) can be analytically described by the conventional Ando formula [97,98],

$$\Delta R_{xx} = 4R_0 D_T \cos\left(\frac{2\pi E_F}{\hbar\omega_c} - \pi\right) \exp\left(-\frac{\pi}{\omega_c\tau_q}\right), \quad \text{(A1)}$$

where ΔR_{xx} is the SdH oscillation amplitude, R_0 is the zero-field resistance, and D_T is the thermal damping factor,

$$D_T = \frac{X_T}{\sinh(X_T)}, \quad X_T = \frac{2\pi^2 k_B T}{\hbar\omega_c}. \quad \text{(A2)}$$

Here k_B is the Boltzmann constant, $\hbar$ is the reduced Planck constant, and T is the bath temperature. In the phase diagram in Fig. 2, the SdH oscillations exhibit two notable features. First, the SdH oscillation amplitude decreases with increasing DC current, and second, an inversion of the SdH oscillation extrema occurs on increasing the DC current further. By fitting the experimental SdH oscillation data to Eq. (A1) it is possible to extract the electron concentration, the quantum lifetime, the amplitude ($4R_0$), and the current dependence of the electron temperature T_e. Note the use of T_e instead of T has been shown [20,99] to be essential to describe the decrease of the SdH oscillation amplitude and the PhI with increasing DC current. We emphasize that for our narrow HB device, there is pronounced nMR around $B = 0$ T [see Fig. 9(a)], and whether one can simply equate R_0 in Eq. (1) for the SdH oscillations [100] with R ($B = 0$ T), the measured value of the zero-field resistance, in this case is important since this impacts the determination of the mobility.

At $I_{DC} = 0$ μA, by fitting the SdH oscillations in Fig. 9(a) to Eq. (A1), we obtain parameters $n = 2.0 \times 10^{11}$ cm^{-2}, $R_0 = 11.4 \pm 0.6$ Ω, and $\tau_q = 11.5 \pm 0.3$ ps. For our experimental conditions, it is possible to detect SdH oscillations up to filling factor $\nu = 2\pi\hbar n/eB$ of 400 [see Fig. 9(b)]. Strongly note that the value of R_0 as determined from SdH is significantly lower than the measured resistance at $B = 0$ T [R(B = 0) = 43 Ω],
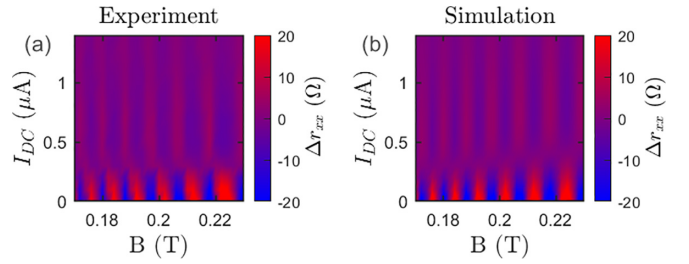

FIG. 10. Colorscale plots showing PhI of the SdH oscillation amplitude Δr_{xx} in r_{xx} data near 0.2 T (a), and a simulation of the data (b). The simulation is generated from Eq. (A3).

indicating that the phenomenon of nMR near zero field is independent from the SdH oscillation effect. Consequently, without accounting for the presence of the nMR (and the double-peak feature superimposed on top of the nMR), taking the R ($B = 0$ T) = 43 Ω value rather than the fitted value of $R_0 = 11.4$ Ω relevant to the SdH oscillations, the estimated mobility would be lower than the bulk mobility by almost a factor of four [101]. We note in our study R_0 is close to the bulk resistance, whereas in other experiments [102] the value of R_0 extracted from SdH oscillations does not necessarily correspond to the resistance at zero field, i.e., for our situation the assumption implicit in the Ando formula that the B-field dependence of the DOS is sinusoidal in nature to first-order is justified.

Away from $I_{DC} = 0$ μA, the SdH oscillation amplitude decreases, and eventually PhI occurs, see Fig. 10 where this takes place at $\sim$0.2 μA near 0.2 T. PhI whereby the extrema of the SdH oscillations invert with increasing DC current was discussed theoretically in Refs. [4,103], and has been reported experimentally for high mobility semiconductor 2DEGs [20,24,76,104–106], and for graphene [99]. For r_{xx}, PhI with increasing DC current can be explained by an electron heating model in terms of the following relation [20],

$$\Delta r_{xx} = \Delta R_{xx} + I_{DC}\frac{\partial \Delta R_{xx}}{\partial T_e}\frac{\partial T_e}{\partial I}, \quad \text{(A3)}$$

derived from $\Delta r_{xx} = d(\Delta R_{xx}I)/dI$, where Δr_{xx} is the SdH oscillation amplitude in the differential resistance, and ΔR_{xx} is the magnetoresistance described in Eq. (A1). The term $\partial \Delta R_{xx}/\partial T_e$ introduces oscillations shifted by a phase of π that dominate at larger I_{DC}. At higher T_e, the damping factor $D(T)$ from Eq. (A2) decreases the amplitude of the SdH oscillations. Taken from the data set shown in full in Fig. 2, Fig. 10(a) shows Δr_{xx} near 0.2 T. Figure 10(b) shows a simulation of the experimental data obtained with Eq. (A3). The simulation assumes the electron temperature is a fitting parameter of the form $T_e(I_{DC}) = T_0 + \alpha I_{DC}^\beta$, where $T_0 = 0.04$ K is the expected electron temperature at zero current, and α and β are constants. The empirical dependence of the electron temperature with DC current is found to be $T_e(I_{DC}) = T_0 + 1.0I_{DC}^{0.65}$ where I_{DC} is in μA. To obtain the parameters α and β, a Monte Carlo approach is used as both T_e and $\partial T_e/\partial I$ need to be fitting parameters in the model. We find $\beta \sim 0.65$ consistent with the value reported in previous work by Studenikin *et al.* [20] in an InGaAs/InP QW HB device with a much smaller carrier mobility of 1.9×10^5 cm^2/Vs. This demonstrates that

electron heating is also an important mechanism for PhI in very high mobility HB devices in the large filling factor regime.

APPENDIX B: NEGATIVE MAGNETORESISTANCE

nMR is commonly observed in high-mobility 2DEG Hall bar devices, [50,59,107–116] and narrow micron-sized quantum devices such as quantum wires and quantum point contacts [117–121]. nMR can arise from different effects. In one limit, nMR is often associated with weak localization (WL), see for example Refs. [109,122,123], which is due to coherent back-scattering with impurities, when the mean free path is small compared to the phase coherence length. nMR also occurs in the opposite (ballistic) regime, when the mean free path is larger than the Hall bar width and the distance between voltage probes, and coherent backscattering is negligible, see for example Refs. [59,107–109,112–115]. Our Hall bar is in this regime, and so the strong nMR we observe in Fig. 9 arises from the ballistic effect.

For a fully ballistic conductor with lateral confinement, the nMR is a direct consequence of the nonzero resistance due to the finite number of quantum channels. In the limiting case, where there is no electron scattering, the two-terminal resistance is simply given by $R_{2T} = h/g_s e^2 N$, where h is the Planck constant, $g_s = 2$ is the spin degeneracy, and N is the number of quantum transmission channels. For a confinement potential $V(y)$ in the transverse direction, the number of channels can be found by using the Bohr-Sommerfeld quantization rule

$$N = \frac{2}{h} \int_{y_1}^{y_2} p \, dy. \tag{B1}$$

Here $p = \sqrt{2m^*(E_F - V(y))}$ is the quasiclassical momentum, and y_1 and y_2 are the boundaries where p is real. For a hard wall confinement potential of width W ($y_1 = -W/2$ and $y_2 = W/2$), and without a B field, this leads to the well-know expression $N = Wk_F/\pi$, where the number of channels is twice the width divided by the Fermi wave length. In the presence of a B field, N is reduced due to Landau quantization, and the quasiclassical momentum is now given by $p = \sqrt{2m^*(E_F - V(y)) - (eBy)^2}$. For a hard-wall confinement potential, Eq. (B1) can be evaluated directly and one obtains

$$N = \frac{Wk_F}{\pi} f\left(\frac{W}{2r_c}\right);$$
$$f(s) = \frac{1}{2}\left(\sqrt{1 - s^2} + \frac{\arcsin s}{s}\right). \tag{B2}$$

Equation (B2) is a generalization to the approximate expression obtained by Glazman and Khaetskii [124], who considered the two limits $W \ll 2r_c$ and $W \gg 2r_c$ separately. In these two limits both expressions coincide. For a smooth confinement potential, N can be obtained by evaluating the integral in Eq. (B1) numerically.

For instance, if we now consider, as depicted in the inset to Fig. 11, an exponential depletion potential of the form

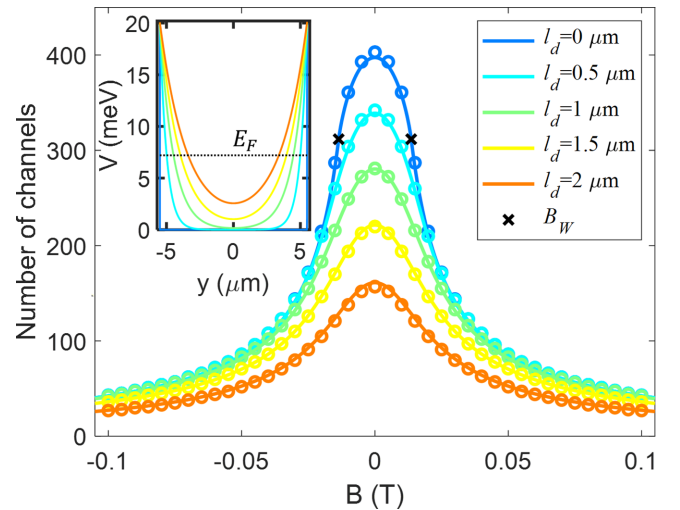$$V(y) = U_0(e^{-|y-y_1|/l_d} + e^{-|y-y_2|/l_d}), \tag{B3}$$

FIG. 11. Calculated number of transmission channels N (proportional to the conductance) as a function of B field for different values of the sidewall depletion length l_d in µm. The lines are obtained using Eq. (B1), while the open dots are obtained by computing the two-terminal transmission numerically using a discretized Schrödinger equation with two semi-infinite leads. The crosses indicate the B fields B_W where $W = 2r_c$. Here a width of $W = 11$ µm is assumed, and we have taken U_0 to be 20 meV. Inset: Calculated depletion potential for a section through the Hall bar for different values of l_d. $l_d = 0$ µm corresponds to a hard-wall potential.

with l_d the depletion length, and U_0 the barrier potential, we can compare the numerically obtained conductance, assuming no diffuse scattering (in the bulk or at the edge of the Hall bar), with Eq. (B1). Both are in excellent agreement as shown in Fig. 11. The most distinctive feature is the rapid decrease of the number of transmission channels with increasing B field. The characteristic field B_W for the rapid decrease is given by $W = 2r_c$ for which the slope of $N(B)$ is maximal. Our simple model therefore can explain the strong nMR observed in Fig. 9(a). However, note that B_W here is closer to the maximum of $N(B)$, while in Fig. 9(a), B_W is further down the side of the nMR. In the Hall bar measured, this is likely due to the presence of diffuse scattering, and the voltage probe regions, both of which are neglected in the simple model and the numerical simulation. Indeed, for a Hall bar in the strong ballistic regime, scattering is dominated by scattering off the openings to the voltage probes along the sides, since no scattering would lead to a zero four-terminal resistance. Scattering from the voltage probes is proportional to N, hence the four-terminal resistance will show a similar B dependence as $N(B)$, leading to the observed nMR. Moreover, in ballistic narrow Hall bars, the two-terminal resistance at $B = 0$ T is bounded by the number of conducting channels, i.e., $R > h/2e^2 N$ ($R > 16$ Ω in our Hall bar), regardless of the scattering potential and Hall bar aspect ratio. As a consequence, the transport mobility (or transport lifetime) cannot be extracted from the measured resistance at $B = 0$ T when nMR is present but only from a fit of the SdH oscillations as discussed in Appendix A.

In addition to the nMR we also observe a dip at $B = 0$ T leading to the distinctive double-peak feature seen in Fig. 2(e).

The double-peak feature has been reported in recent experiments on narrow channels in 2D metals [61], and nanowires in graphene [125], and was attributed to ballistic transport. The double-peak feature has also been discussed elsewhere both theoretically [66] and experimentally [43,125,126], where the peaks were reported to occur at W $\simeq 0.55r_c$. For our Hall bar device, we infer $W_{\text{eff}} \simeq 0.65r_c$ from the position of the two peaks in the double-peak feature at zero DC current (B $\sim \pm 4.7$ mT). In the calculation displayed in Fig. 11 no double-peak feature is visible. We found that whether a double-peak feature appears in a calculation or not depends sensitively on the details of the boundary scattering assumed, and is more prominent with diffuse scattering on the edge along the Hall bar channel [118]. For the calculation relevant to Fig. 11 we assumed no diffuse scattering at the edge nor in the bulk. We strongly note that because we are in the regime $W \ll l_{mfp} \sim 145$ μm, the nMR and double-peak feature we observe are ballistic in origin and do not arise from a combination of WL and weak antilocalization (WAL) [127]. In GaAs/AlGaAs heterostructures spin-orbit interaction is weak, and even in the case of a moderate mobility 2DEG where WL and WAL have been observed to co-exist, the resulting double-peak feature is tightly confined within ± 0.1 mT of zero field [128].

[1] R. E. Prange and S. M. Girvin, eds., *The Quantum Hall Effect* (Springer, New York, 1990)

[2] T. Chakraborty and P. Pietiläinen, *The Quantum Hall Effects* (Springer, Berlin, 1995).

[3] I. A. Dmitriev, A. D. Mirlin, D. G. Polyakov, and M. A. Zudov, Rev. Mod. Phys. **84**, 1709 (2012).

[4] S. Vitkalov, Int. J. Mod. Phys. B **23**, 4727 (2009).

[5] C. L. Yang, J. Zhang, R. R. Du, J. A. Simmons, and J. L. Reno, Phys. Rev. Lett. **89**, 076801 (2002).

[6] A. A. Bykov, J.-q. Zhang, S. Vitkalov, A. K. Kalagin, and A. K. Bakarov, Phys. Rev. B **72**, 245307 (2005).

[7] W. Zhang, M. A. Zudov, L. N. Pfeiffer, and K. W. West, Phys. Rev. Lett. **98**, 106804 (2007).

[8] J. Q. Zhang, S. Vitkalov, A. A. Bykov, A. K. Kalagin, and A. K. Bakarov, Phys. Rev. B **75**, 081305(R) (2007).

[9] W. Zhang, H.-S. Chiang, M. A. Zudov, L. N. Pfeiffer, and K. W. West, Phys. Rev. B **75**, 041304(R) (2007).

[10] A. A. Bykov, Sov. Phys. JETP **88**, 394 (2008).

[11] Y. Dai, Z. Q. Yuan, C. L. Yang, R. R. Du, M. J. Manfra, L. N. Pfeiffer, and K. W. West, Phys. Rev. B **80**, 041310(R) (2009).

[12] A. T. Hatke, M. A. Zudov, L. N. Pfeiffer, and K. W. West, Phys. Rev. B **79**, 161308(R) (2009).

[13] A. T. Hatke, H.-S. Chiang, M. A. Zudov, L. N. Pfeiffer, and K. W. West, Phys. Rev. B **82**, 041304(R) (2010).

[14] A. T. Hatke, M. A. Zudov, L. N. Pfeiffer, and K. W. West, Phys. Rev. B **83**, 081301(R) (2011).

[15] A. Bykov, D. Dmitriev, I. Marchishin, S. Byrnes, and S. Vitkalov, Appl. Phys. Lett. **100**, 251602 (2012).

[16] S. Wiedmann, G. M. Gusev, O. E. Raichev, A. K. Bakarov, and J. C. Portal, Phys. Rev. B **84**, 165303 (2011).

[17] Q. Shi, M. A. Zudov, J. Falson, Y. Kozuka, A. Tsukazaki, M. Kawasaki, K. von Klitzing, and J. Smet, Phys. Rev. B **95**, 041411(R) (2017).

[18] M. A. Zudov, I. A. Dmitriev, B. Friess, Q. Shi, V. Umansky, K. von Klitzing, and J. Smet, Phys. Rev. B **96**, 121301(R) (2017).

[19] J. Mi, H. Liu, J. Shi, L. N. Pfeiffer, K. W. West, K. W. Baldwin, and C. Zhang, Phys. Rev. B **100**, 235437 (2019).

[20] S. A. Studenikin, G. Granger, A. Kam, A. S. Sachrajda, Z. R. Wasilewski, and P. J. Poole, Phys. Rev. B **86**, 115309 (2012).

[21] K. Panos, R. Gerhardts, J. Weis, and K. Von Klitzing, New J. Phys. **16**, 113071 (2014).

[22] S. Baer, C. Rössler, S. Hennel, H. C. Overweg, T. Ihn, K. Ensslin, C. Reichl, and W. Wegscheider, Phys. Rev. B **91**, 195414 (2015).

[23] A. V. Rossokhaty, Y. Baum, J. A. Folk, J. D. Watson, G. C. Gardner, and M. J. Manfra, Phys. Rev. Lett. **117**, 166805 (2016).

[24] V. Yu, M. Hilke, P. J. Poole, S. Studenikin, and D. G. Austing, Phys. Rev. B **98**, 165434 (2018).

[25] R. Gurzhi, Sov. Phys. JETP **44**, 771 (1963).

[26] R. Gurzhi, Sov. Phys. Usp. **11**, 255 (1968).

[27] G. F. Giuliani and J. J. Quinn, Phys. Rev. B **26**, 4421 (1982).

[28] R. Gurzhi, A. Kalinenko, and A. Kopeliovich, Sov. Phys. JETP **69**, 863 (1989).

[29] R. Jaggi, J. Appl. Phys. **69**, 816 (1991).

[30] L. W. Molenkamp and M. J. M. de Jong, Phys. Rev. B **49**, 5038 (1994).

[31] M. J. M. de Jong and L. W. Molenkamp, Phys. Rev. B **51**, 13389 (1995).

[32] L. Molenkamp and M. de Jong, Solid State Electron. **37**, 551 (1994).

[33] L. Eaves, Phys. B: Condens. Matter **256-258**, 47 (1998).

[34] L. Eaves, Phys. B: Condens. Matter **272**, 130 (1999).

[35] L. Eaves, S. Stoddart, R. Wirtz, A. Neumann, B. Gallagher, P. Main, and M. Henini, Physica E **6**, 136 (2000).

[36] L. Eaves, Physica E **9**, 45 (2001).

[37] L. Eaves, Phys. B: Condens. Matter **298**, 1 (2001).

[38] A. Martin, K. Benedict, F. Sheard, and L. Eaves, Physica E **22**, 205 (2004).

[39] J. Zaanen, Science **351**, 1026 (2016).

[40] D. A. Bandurin, I. Torre, R. K. Kumar, M. B. Shalom, A. Tomadin, A. Principi, G. H. Auton, E. Khestanova, K. S. Novoselov, I. V. Grigorieva *et al.*, Science **351**, 1055 (2016).

[41] J. Crossno, J. K. Shi, K. Wang, X. Liu, A. Harzheim, A. Lucas, S. Sachdev, P. Kim, T. Taniguchi, K. Watanabe *et al.*, Science **351**, 1058 (2016).

[42] L. Levitov and G. Falkovich, Nat. Phys. **12**, 672 (2016).

[43] J. A. Sulpizio, L. Ella, A. Rozen, J. Birkbeck, D. J. Perello, D. Dutta, M. Ben-Shalom, T. Taniguchi, K. Watanabe, T. Holder *et al.*, Nature (London) **576**, 75 (2019).

[44] A. I. Berdyugin, S. G. Xu, F. M. D. Pellegrino, R. K. Kumar, A. Principi, I. Torre, M. B. Shalom, T. Taniguchi, K. Watanabe, I. V. Grigorieva *et al.*, Science **364**, 162 (2019).

[45] P. Gallagher, C.-S. Yang, T. Lyu, F. Tian, R. Kou, H. Zhang, K. Watanabe, T. Taniguchi, and F. Wang, Science **364**, 158 (2019).

[46] L. Ella, A. Rozen, J. Birkbeck, M. Ben-Shalom, D. Perello, J. Zultak, T. Taniguchi, K. Watanabe, A. K. Geim, S.

Ilani, and J. A. Sulpizio, Nat. Nanotechnol. **14**, 480 (2019).

[47] M. J. H. Ku, T. X. Zhou, Q. Li, Y. J. Shin, J. K. Shi, C. Burch, L. E. Anderson, A. T. Pierce, Y. Xie, A. Hamo *et al.*, Nature (London) **583**, 537 (2020).

[48] Y. A. Pusep, M. D. Teodoro, V. Laurindo, E. R. Cardozo de Oliveira, G. M. Gusev, and A. K. Bakarov, Phys. Rev. Lett. **128**, 136801 (2022).

[49] A. Jenkins, S. Baumann, H. Zhou, S. A. Meynell, Y. Daipeng, K. Watanabe, T. Taniguchi, A. Lucas, A. F. Young, and A. C. Bleszynski Jayich, Phys. Rev. Lett. **129**, 087701 (2022).

[50] Q. Shi, P. D. Martin, Q. A. Ebner, M. A. Zudov, L. N. Pfeiffer, and K. W. West, Phys. Rev. B **89**, 201301(R) (2014).

[51] G. M. Gusev, A. D. Levin, E. V. Levinson, and A. K. Bakarov, Phys. Rev. B **98**, 161303(R) (2018).

[52] A. D. Levin, G. M. Gusev, E. V. Levinson, Z. D. Kvon, and A. K. Bakarov, Phys. Rev. B **97**, 245308 (2018).

[53] G. M. Gusev, A. D. Levin, E. V. Levinson, and A. K. Bakarov, AIP Adv. **8**, 025318 (2018).

[54] B. A. Braem, F. M. D. Pellegrino, A. Principi, M. Röösli, C. Gold, S. Hennel, J. V. Koski, M. Berl, W. Dietsche, W. Wegscheider, M. Polini, T. Ihn, and K. Ensslin, Phys. Rev. B **98**, 241304(R) (2018).

[55] G. M. Gusev, A. S. Jaroshevich, A. D. Levin, Z. D. Kvon, and A. K. Bakarov, Sci. Rep. **10**, 7860 (2020).

[56] A. C. Keser, D. Q. Wang, O. Klochan, D. Y. H. Ho, O. A. Tkachenko, V. A. Tkachenko, D. Culcer, S. Adam, I. Farrer, D. A. Ritchie, O. P. Sushkov, and A. R. Hamilton, Phys. Rev. X **11**, 031030 (2021).

[57] A. Gupta, J. J. Heremans, G. Kataria, M. Chandra, S. Fallahi, G. C. Gardner, and M. J. Manfra, Phys. Rev. Lett. **126**, 076803 (2021).

[58] A. N. Afanasiev, P. S. Alekseev, A. A. Greshnov, and M. A. Semina, Phys. Rev. B **104**, 195415 (2021).

[59] B. Horn-Cosfeld, J. Schluck, J. Lammert, M. Cerchez, T. Heinzel, K. Pierz, H. W. Schumacher, and D. Mailly, Phys. Rev. B **104**, 045306 (2021).

[60] E. Mönch, S. O. Potashin, K. Lindner, I. Yahniuk, L. E. Golub, V. Y. Kachorovskii, V. V. Bel'kov, R. Huber, K. Watanabe, T. Taniguchi, J. Eroms, D. Weiss, and S. D. Ganichev, Phys. Rev. B **105**, 045404 (2022).

[61] P. J. W. Moll, P. Kushwaha, N. Nandi, B. Schmidt, and A. P. Mackenzie, Science **351**, 1061 (2016).

[62] A. Aharon-Steinberg, T. Völkl, A. Kaplan, A. K. Pariari, I. Roy, T. Holder, Y. Wolf, A. Y. Meltzer, Y. Myasoedov, M. E. Huber *et al.*, Nature (London) **607**, 74 (2022).

[63] J. Gooth, F. Menges, N. Kumar, V. Süss, C. Shekhar, Y. Sun, U. Drechsler, R. Zierold, C. Felser, and B. Gotsmann, Nat. Commun. **9**, 4093 (2018).

[64] P. S. Alekseev, Phys. Rev. Lett. **117**, 166601 (2016).

[65] H. Guo, E. Ilseven, G. Falkovich, and L. S. Levitov, Proc. Natl. Acad. Sci. USA **114**, 3068 (2017).

[66] T. Scaffidi, N. Nandi, B. Schmidt, A. P. Mackenzie, and J. E. Moore, Phys. Rev. Lett. **118**, 226601 (2017).

[67] P. S. Alekseev and M. A. Semina, Phys. Rev. B **100**, 125419 (2019).

[68] P. S. Alekseev and A. P. Alekseeva, Phys. Rev. Lett. **123**, 236801 (2019).

[69] P. S. Alekseev and A. P. Dmitriev, Phys. Rev. B **102**, 241409(R) (2020).

[70] I. Matthaiakakis, D. Rodríguez Fernández, C. Tutschku, E. M. Hankiewicz, J. Erdmenger, and R. Meyer, Phys. Rev. B **101**, 045423 (2020).

[71] O. E. Raichev, G. M. Gusev, A. D. Levin, and A. K. Bakarov, Phys. Rev. B **101**, 235314 (2020).

[72] S. Ahn and S. Das Sarma, Phys. Rev. B **106**, L081303 (2022).

[73] A. N. Afanasiev, P. S. Alekseev, A. A. Danilenko, A. P. Dmitriev, A. A. Greshnov, and M. A. Semina, Phys. Rev. B **106**, 245415 (2022).

[74] M. Hara, A. Endo, S. Katsumoto, and Y. Iye, Phys. Rev. B **69**, 153304 (2004).

[75] W. Pan, J. Xia, H. Stormer, D. Tsui, C. Vicente, E. Adams, N. Sullivan, L. Pfeiffer, K. Baldwin, and K. West, Solid State Commun. **140**, 88 (2006).

[76] J. Q. Zhang, S. Vitkalov, and A. A. Bykov, Phys. Rev. B **80**, 045310 (2009).

[77] In our measurements, we are in a regime where hydrodynamics is a small correction that can be quantified by the parameter r_H, which is always smaller than 0.03 as shown in Fig. 4(d). If r_H were close to unity we would expect a full hydrodynamic behavior in the Poiseuille regime. Our study is thus in the regime where the hydrodynamic correction is small but induced to grow by applying a DC current. We are essentially at the border (or crossover) between the pure ballistic and pure hydrodynamic (Poiseulle) regimes as discussed in Ref. [43]. Since in our experiment the hydrodynamic component is only a small correction, any assumption of uniform or parabolic current profile would not affect much the estimate of τ_{ee}. Moreover, our experiments do not allow us to probe the spatial distribution of the current distribution. That being said, we estimate the Gurzhi length following Ref. [43] to be $\sqrt{l_{ee}l_{mfp}}/2 \simeq 23$ μm at the highest current of 10 μA, which is larger than the width of our Hall bar.

[78] P. Y. Yu and M. Cardona, *Fundamentals of Semiconductors* (Springer, Berlin, 2005) p. 207.

[79] A. V. Chaplik, Sov. Phys. JETP **33**, 997 (1971).

[80] A. Yacoby, U. Sivan, C. P. Umbach, and J. M. Hong, Phys. Rev. Lett. **66**, 1938 (1991).

[81] Fitting the empirical parabolic dependence reflected in Eq. (1) with Eq. (2), we find $\Delta = 0.88 eV_{DC}$, which is close to $\Delta = 0.82 eV_{DC}$ obtained by Yacoby *et al.* in Ref. [80].

[82] R. Krishna Kumar, D. Bandurin, F. Pellegrino, Y. Cao, A. Principi, H. Guo, G. Auton, M. Ben Shalom, L. A. Ponomarenko, G. Falkovich *et al.*, Nat. Phys. **13**, 1182 (2017).

[83] R. J. Blaikie, D. R. S. Cumming, J. R. A. Cleaver, H. Ahmed, and K. Nakazato, J. Appl. Phys. **78**, 330 (1995).

[84] M. G. Vavilov and I. L. Aleiner, Phys. Rev. B **69**, 035303 (2004).

[85] I. A. Dmitriev, M. G. Vavilov, I. L. Aleiner, A. D. Mirlin, and D. G. Polyakov, Phys. Rev. B **71**, 115316 (2005).

[86] M. G. Vavilov, I. L. Aleiner, and L. I. Glazman, Phys. Rev. B **76**, 115331 (2007).

[87] M. Khodas and M. G. Vavilov, Phys. Rev. B **78**, 245319 (2008).

[88] S. A. Studenikin, M. Potemski, A. Sachrajda, M. Hilke, L. N. Pfeiffer, and K. W. West, Phys. Rev. B **71**, 245313 (2005).

[89] A. T. Hatke, H.-S. Chiang, M. A. Zudov, L. N. Pfeiffer, and K. W. West, Phys. Rev. Lett. **101**, 246811 (2008).

[90] We can give an estimate of the electron temperature T_e from the phase inversion data (see Appendix A), which is best fit with $T_e = 0.04 + I_{DC}^{0.65} \simeq 4.5$ K at 10 μA. In comparison to experiments at elevated bath temperature, such as that reported by Gusev *et al.* [51] where the hydrodynamic contribution is studied for temperatures between 1.7–40 K, even at the highest current applied (10 μA), the current-induced effective heating in our case is still at the low end of temperature range they studied. Nevertheless, both approaches are consistent, in the sense that our observed current-induced hydrodynamic contribution and the extracted effective temperature overlap with previous experiments where hydrodynamics was induced solely with an elevated bath temperature.

[91] In our experiments Joule heating due to the applied DC current is minimal since the estimated DC power is less than 80 nW, which is very small compared to the bath cooling power of the dilution refrigerator at base temperature. We also do not observe any heating in the thermometer attached to the mixing chamber plate at small magnetic fields [$B < 0.25$ T for the full phase diagram in Fig. 2(a)] where the two-terminal resistance remains less than 800 Ω. The situation would be different at higher magnetic fields, where the two-terminal resistance can be much larger, which would lead to some Joule heating, but this is not relevant to the hydrodynamic regime, which is confined to very small magnetic fields (principally $B < 10$ mT). Also, at the temperature of the dilution refrigerator for which our measurements were performed, up to the maximum DC current applied, we do not observe phonon-induced resistance oscillations a phenomenon only seen clearly at elevated (bath) temperatures- see Ref. [3].

[92] X. Wang, P. Jia, R.-R. Du, L. N. Pfeiffer, K. W. Baldwin, and K. W. West, Phys. Rev. B **106**, L241302 (2022).

[93] T. Ando, J. Phys. Soc. Jpn. **36**, 1521 (1974).

[94] T. Ando, J. Phys. Soc. Jpn. **37**, 1233 (1974).

[95] T. Ando, J. Phys. Soc. Jpn. **38**, 989 (1975).

[96] T. Ando, J. Phys. Soc. Jpn. **51**, 3900 (1982).

[97] P. T. Coleridge, Phys. Rev. B **44**, 3793 (1991).

[98] A. Isihara and L. Smrcka, J. Phys. C: Solid State Phys. **19**, 6777 (1986).

[99] Z. Tan, C. Tan, L. Ma, G. T. Liu, L. Lu, and C. L. Yang, Phys. Rev. B **84**, 115429 (2011).

[100] F. B. Mancoff, L. J. Zielinski, C. M. Marcus, K. Campman, and A. C. Gossard, Phys. Rev. B **53**, R7599(R) (1996).

[101] The electron mobility measured at 0.28 K for a large area Van der Pauw device in which we expect nMR arising from ballistic transport to be negligible is 20×10^6 cm^2/V s. For the narrow Hall bar measured at the dilution refrigerator base temperature, from fitting the SdH oscillations in Fig. 9(b), we extracted $R_0 = 11.4$ Ω which corresponds to an electron mobility of 25×10^6 cm^2/V s. Independently, from the plot of the SdH oscillation extrema amplitudes in Fig. 7(c), we obtain $R_0 = 13.5$ Ω, which corresponds to an electron mobility of 22×10^6 cm^2/V s.

[102] P. T. Coleridge, M. Hayne, P. Zawadzki, and A. S. Sachrajda, Surf. Sci. **361-362**, 560 (1996).

[103] I. A. Dmitriev, J. Phys.: Conf. Ser. **334**, 012015 (2011).

[104] N. R. Kalmanovitz, A. A. Bykov, S. Vitkalov, and A. I. Toropov, Phys. Rev. B **78**, 085306 (2008).

[105] J. A. Alexander-Webber, A. M. R. Baker, P. D. Buckle, T. Ashley, and R. J. Nicholas, Phys. Rev. B **86**, 045404 (2012).

[106] S. Dietrich, S. Byrnes, S. Vitkalov, D. V. Dmitriev, and A. A. Bykov, Phys. Rev. B **85**, 155307 (2012).

[107] L. Bockhorn, A. Hodaei, D. Schuh, W. Wegscheider, and R. J. Haug, J. Phys.: Conf. Ser. **456**, 012003 (2013).

[108] A. T. Hatke, M. A. Zudov, J. L. Reno, L. N. Pfeiffer, and K. W. West, Phys. Rev. B **85**, 081304(R) (2012).

[109] R. G. Mani, A. Kriisa, and W. Wegscheider, Sci. Rep. **3**, 2747 (2013).

[110] Z. Wang, R. L. Samaraweera, C. Reichl, W. Wegscheider, and R. G. Mani, Sci. Rep. **6**, 38516 (2016).

[111] R. L. Samaraweera, H.-C. Liu, Z. Wang, C. Reichl, W. Wegscheider, and R. G. Mani, Sci. Rep. **7**, 5074 (2017).

[112] R. L. Samaraweera, H.-C. Liu, B. Gunawardana, A. Kriisa, C. Reichl, W. Wegscheider, and R. G. Mani, Sci. Rep. **8**, 10061 (2018).

[113] R. L. Samaraweera, B. Gunawardana, T. R. Nanayakkara, R. C. Munasinghe, A. Kriisa, C. Reichl, W. Wegscheider, and R. G. Mani, Sci. Rep. **10**, 781 (2020).

[114] M. A. Zudov, I. V. Ponomarev, A. L. Efros, R. R. Du, J. A. Simmons, and J. L. Reno, Phys. Rev. Lett. **86**, 3614 (2001).

[115] L. Bockhorn, P. Barthold, D. Schuh, W. Wegscheider, and R. J. Haug, Phys. Rev. B **83**, 113301 (2011).

[116] L. Bockhorn, I. V. Gornyi, D. Schuh, C. Reichl, W. Wegscheider, and R. J. Haug, Phys. Rev. B **90**, 165434 (2014).

[117] K. K. Choi, D. C. Tsui, and S. C. Palmateer, Phys. Rev. B **33**, 8216 (1986).

[118] T. J. Thornton, M. L. Roukes, A. Scherer, and B. P. Van de Gaag, Phys. Rev. Lett. **63**, 2128 (1989).

[119] P. H. M. van Loosdrecht, C. W. J. Beenakker, H. Van Houten, J. G. Williamson, B. J. Van Wees, J. E. Mooij, C. T. Foxon, and J. J. Harris, Phys. Rev. B **38**, 10162 (1988).

[120] H. van Houten, C. W. J. Beenakker, P. H. M. Van Loosdrecht, T. J. Thornton, H. Ahmed, M. Pepper, C. T. Foxon, and J. J. Harris, Phys. Rev. B **37**, 8534 (1988).

[121] R. G. Mani, K. von Klitzing, and K. Ploog, Phys. Rev. B **48**, 4571 (1993).

[122] M. Paalanen, D. Tsui, B. Lin, and A. Gossard, Surf. Sci. **142**, 29 (1984).

[123] B. Kramer and A. MacKinnon, Rep. Prog. Phys. **56**, 1469 (1993).

[124] L. Glazman and A. Khaetskii, J. Phys.: Condens. Matter **1**, 5005 (1989).

[125] S. Masubuchi, K. Iguchi, T. Yamaguchi, M. Onuki, M. Arai, K. Watanabe, T. Taniguchi, and T. Machida, Phys. Rev. Lett. **109**, 036601 (2012).

[126] E. Ditlefsen and J. Lothe, Philos. Mag. **14**, 759 (1966).

[127] S. Hikami, A. I. Larkin, and Y. Nagaoka, Prog. Theor. Phys. **63**, 707 (1980).

[128] J. B. Miller, D. M. Zumbühl, C. M. Marcus, Y. B. Lyanda-Geller, D. Goldhaber-Gordon, K. Campman, and A. C. Gossard, Phys. Rev. Lett. **90**, 076807 (2003).